Research Square

Preprints are preliminary reports that have not undergone peer review.
They should not be considered conclusive, used to inform clinical practice,
or referenced by the media as validated information.

Human Immune State-Guided Biomimetic Nanoadjuvant Reprograms Tumor-Draining Lymph Nodes to Enhance Cancer Immunotherapy

Xin Zhang
The First Hospital of China Medical University
Tiantongfei Jiang
Harbin Medical University
Lingxiao Zhao
Health Sciences Institute of China Medical University
Yuxin Wan
Harbin Medical University
Chan Li
Health Sciences Institute of China Medical University
Yaru Niu
Cancer Hospital of Chinese Academy of Medical Sciences
Jian Ma
Beijing Shijitan Hospital
Juan Xu
Harbin Medical University
Xu Guan
Cancer Hospital of Chinese Academy of Medical Sciences
Xishan Wang
wangxishan@cicams.ac.cn

Cancer Hospital of Chinese Academy of Medical Sciences

Research Article

Keywords: Lymph node, Dendritic cells, Biomimetic nanoadjuvant, Cancer immunotherapy

Posted Date: November 17th, 2026

DOI: https://doi.org/10.21203/rs.3.rs-11589045/v1

License: This work is licensed under a Creative Commons Attribution 4.0 International License.
Read Full License

Additional Declarations: No competing interests reported.

Human Immune State-Guided Biomimetic Nanoadjuvant Reprograms Tumor-Draining Lymph Nodes to Enhance Cancer Immunotherapy

*Xin Zhang [2, #], Tiantongfei Jiang [3, #], Lingxiao Zhao [4, #], Yuxin Wan [3 #], Chan Li [4], Yaru Niu [1], Jian Ma [5], Juan Xu [3 *], Xu Guan [1, *], Xishan Wang [1, 2 *]*

[1]Department of Colorectal Surgery, National Cancer Center/National Clinical Research Center for Cancer/Cancer Hospital, Chinese Academy of Medical Sciences & Peking Union Medical College, Beijing 100124, China.

[2] Department of Surgical Oncology and General Surgery, The First Hospital of China Medical University, Shenyang, 110122, China.

[3]College of Bioinformatics Science and Technology, Harbin Medical University, Harbin 150081, China.

[4]Key Laboratory of Medical Cell Biology of Ministry of Education, Key Laboratory of Major Chronic Diseases of Nervous System of Liaoning Province, Health Sciences Institute of China Medical University, Shenyang, 110122, China.

[5]Department of Peritoneal Cancer Surgery, Beijing Shijitan Hospital, Capital Medical University, Beijing, 100038, China.

[#]These authors contributed equally to this work.

[*]Correspondence should be addressed to Juan Xu (email: xujuanbiocc@ems.hrbmu.edu.cn), Xu Guan (email: guanxu@cicams.ac.cn) and Xishan Wang (email: wangxishan@cicams.ac.cn).

Keywords:
Lymph node; Dendritic cells; Biomimetic nanoadjuvant; Cancer immunotherapy

Abstract: Effective antitumor immunity depends on immune priming within tumor-draining lymph nodes (TDLNs), yet therapeutic strategies targeting these immune-organizing sites remain limited. Here, we leveraged single-cell profiling of human colorectal cancer TDLNs to guide the design of a biomimetic nanoadjuvant for TDLN-targeted cancer immunotherapy. Single-cell and bulk transcriptomic analyses identified a $LAMP3^+$ dendritic cell (DC) state associated with enhanced antigen presentation, costimulation, innate immune sensing, and antigen-experienced $CD8^+$ T cell responses. Inspired by this human immune state, we engineered a DC membrane coated iridium-manganese oxide nanoadjuvant (IMOD NAs) loaded with ovalbumin (OVA) that integrates biomimetic recognition with coordinated redox and innate immune regulation. The DC membrane camouflage enhanced TDLN targeting, DC interaction and OVA delivery, whereas the IrMn oxide core simultaneously activated ROS-NF-κB and Mn^{2+}-dependent STING signaling, thereby promoting DC maturation, migration, and antigen presentation. Remarkably, IMOD NAs reprogrammed TDLNs toward an immune-competent state, enhanced cytotoxic $CD8^+$ T cell priming, and reduced regulatory T cell accumulation. In vivo, IMOD NAs suppressed tumor growth and markedly enhanced the therapeutic efficacy of PD-L1 blockade. Taken together, this study establishes a human immune state guided strategy for biomimetic nanoadjuvant design and demonstrates TDLN reprogramming as a complementary approach to improve cancer immunotherapy.

Introduction

Immunotherapy is transforming the treatment landscape for patients with cancer, yet its clinical benefits remain largely confined to a subset of patients with sufficiently immunogenic tumors[1-2]. Conventional studies of cancer immunotherapy have primarily focused on the primary tumor and its microenvironment, seeking to restore antitumor immunity by relieving immunosuppression, enhancing effector T cell activity, or improving tumor antigen presentation[3]. However, effective antitumor immunity is not initiated within the tumor itself. Rather, lymph nodes serve as critical sites for immune priming, where tumor-derived antigens and inflammatory signals are received and dendritic cells (DCs) interact with naive T cells to establish tumor-specific T cell responses[4-5]. Thus, the efficacy of immunotherapy is determined not only by the immune landscape of the tumor but also, critically, by the capacity of tumor-draining lymph nodes (TDLNs) to initiate and sustain antitumor immunity[6-7].

The immune status of lymph nodes is highly heterogeneous, and not all lymph nodes are equally competent in supporting effective immune responses[8]. This notion is directly supported by our previous work[9]. Through bulk RNA sequencing and single-cell RNA sequencing analyses of 630 lymph node samples, we found that lymph nodes traditionally classified within the same category-negative lymph nodes-display substantial molecular and immunological heterogeneity. Immunosuppressed lymph nodes were characterized by markedly reduced T- and B-cell activity, stromal expansion, and diminished DC abundance, all of which were strongly associated with poorer patient survival. More importantly, we found that immune checkpoint inhibitor (ICI) therapy could partially restore DC function in these lymph nodes, indicating that lymph node immune dysfunction is not irreversible but represents a therapeutically plastic state. These findings suggest that defining key immune states within lymph nodes and developing strategies to precisely modulate them

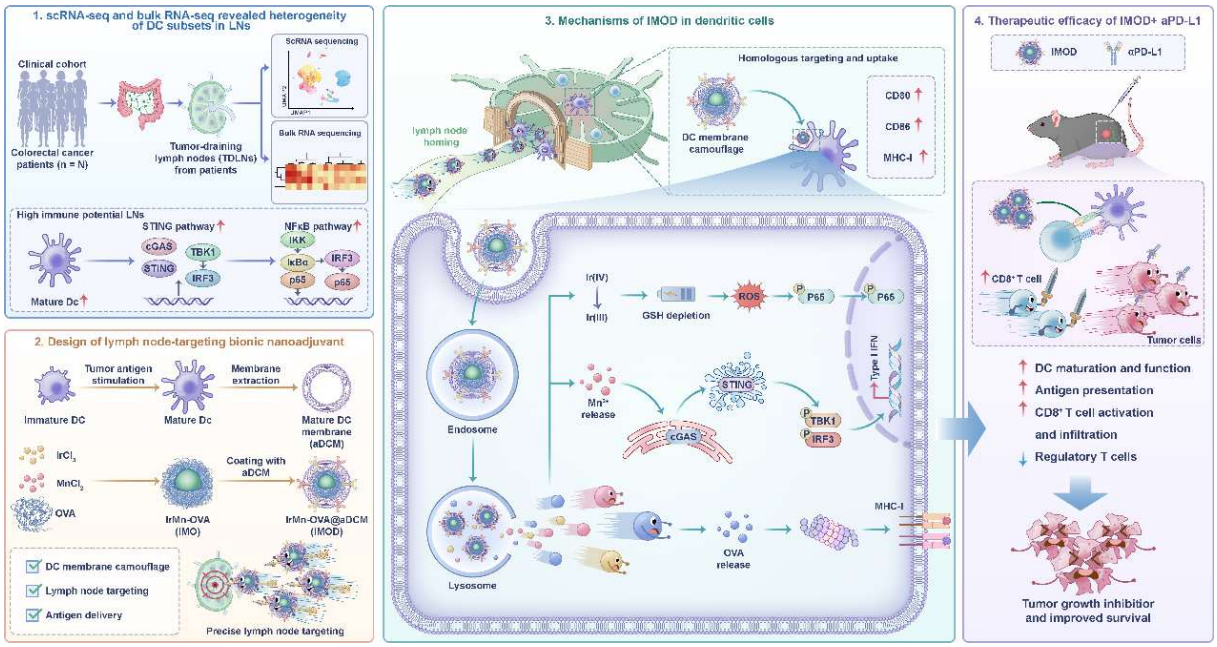
may provide an important avenue for improving cancer immunotherapy[7-9].

This immune heterogeneity is, to a large extent, shaped by tumors. During tumor progression, the persistent influx of tumor-derived antigens and immunosuppressive signals can progressively compromise the immune competence of draining lymph nodes[8-9]. DCs are central to this process. By capturing and presenting tumor antigens while providing costimulatory and inflammatory signals, DCs connect the immune state of lymph nodes to the initiation of antitumor T cell responses[10-12]. Numerous studies have shown that dysfunctional DCs within lymph nodes can substantially impair effective T cell activation and thereby limit therapeutic responses to immunotherapy[11-13, 17]. However, DCs do not constitute a functionally homogeneous population. Instead, they comprise distinct subsets with divergent transcriptional programs and immunological functions[14-16]. Identifying the DC subset most closely associated with productive immune activation is therefore essential for understanding, and ultimately manipulating, the immune competence of tumor-associated lymph nodes.

In parallel, nanomaterials have been extensively explored in cancer immunotherapy to enhance antitumor immune responses through antigen delivery, lymph node targeting, DC activation, and modulation of innate immune pathways such as STING and TLR signaling[18-20]. Nevertheless, the design of most immunomodulatory nanomaterials continues to rely on predefined molecular targets or individual signaling pathways. For instance, Shae et al. developed endosomolytic polymersomes to facilitate the cytosolic delivery of cGAMP, thereby enhancing STING signaling in the tumor microenvironment and sentinel lymph nodes[21]. Wan et al. conjugated the TLR7 agonist 1V209 with cholesterol and formulated it into liposomes to promote lymph node accumulation and activate DC-mediated antitumor immunity while reducing systemic immune toxicity[22]. Similarly, Han et al. engineered a tumor-targeted RNAi nanoblocker to silence PD-L1 in cancer cells, thereby directly interfering with a predefined immune checkpoint pathway[23].

Although these strategies can efficiently activate specific immune programs, they often fail to recapitulate the coordinated and multifunctional states of bona fide immune cells[25-26]. More importantly, the design of such materials is rarely guided by immune states directly identified in human diseased tissues, which may represent a major barrier to their clinical translation[24, 27-30].

Here, we propose a materials-design strategy guided by immune states identified directly in human lymph nodes **(Scheme 1)**. Rather than developing nanomaterials around predefined molecular targets, we first analyzed single-cell transcriptomic data from tumor-associated lymph nodes of patients with colorectal cancer to define the cellular states and functional features associated with effective immune activation. This analysis identified $LAMP3^+$ aDCs as a DC population with prominent immune-activating characteristics. We then translated these functional features into the design of nanoadjuvant (IrMn-OVA@aDCM, IMOD NAs), a DC-membrane-camouflage nanoadjuvant engineered to reconstitute the corresponding immune-activating state within lymph nodes, the primary sites of immune priming. In this way, our study establishes a translational framework that connects discoveries from human clinical samples with functional material design, converting complex human immune cell states into engineerable material properties. This strategy provides a materials-based approach for targeting and remodeling tumor-draining lymph nodes and offers a broader paradigm for designing immunomodulatory materials based on disease-relevant human immune states.



Scheme 1. Schematic illustration of the scRNA-seq guided the design of biomimetic nanoadjuvants and enhances cancer immunotherapy mechanism. (1) scRNA-seq and bulk RNA-seq reveals characteristics of immune-active LNs. (2) Synthesis route of IMOD NAs (inspired by the dendritic cells of immune-active LNs). (3) Mechanisms of IMOD NAs in dendritic cells. (4) IMOD NAs combined with αPD-L1 to enhance immunotherapy.

1. Methods

Sample collection and processing

Fresh tissue specimens were collected immediately after surgical resection. LNs were bisected, with approximately one-third to one-half of each specimen allocated for research and the remaining tissue processed as formalin-fixed, paraffin-embedded material for routine pathological examination. For single-cell preparation, fresh tissues were cut into approximately 1 mm^3 pieces in RPMI-1640 medium containing 10% fetal bovine serum and enzymatically dissociated at 37°C for 30 min using a MACS Tumor Dissociation Kit. Cell suspensions were filtered through a 70 μm cell strainer and centrifuged at 400 × g for 5 min. Red blood cells were removed using red blood cell lysis buffer, and the cells were washed with PBS and resuspended in sorting buffer. Viable cells were identified by 7-AAD staining and isolated by fluorescence-

activated cell sorting. Single-cell libraries were subsequently prepared using the 10x Genomics 3′ single-cell platform according to the manufacturer's instructions and sequenced on an Illumina platform.

Single-cell RNA-seq data processing and cell type annotation

Single-cell RNA-seq data were processed using the Seurat R package. Low-quality cells were removed before normalization and identification of highly variable genes. Principal component analysis and graph-based clustering were subsequently performed, and batch effects across samples were corrected before Uniform manifold approximation and projection (UMAP) visualization. Cell types were assigned according to canonical marker genes and cluster specific expression profiles. Major cell populations were first identified and subsequently reclustered to resolve transcriptionally distinct subpopulations.

DC subset identification and functional analysis

DCs were extracted and reclustered into $IDO1^+$ cDC1, $LAMP3^+$ activated DCs (aDCs), $CLEC10A^+$ cDC2, and $LILRA4^+$ plasmacytoid DCs (pDCs). The activated phenotype of aDCs was characterized by the expression of LAMP3 and CD80. Differentially expressed genes between aDCs and other DC subsets were identified using a two-sided Wilcoxon rank-sum test. Genes enriched in aDCs were subjected to Gene Ontology enrichment analysis using the clusterProfiler R package. Functional scores for cGAS-STING signaling, oxidative stress, lymphocyte costimulation, major histocompatibility complex class I (MHC-I) antigen presentation, and DC maturation were calculated using predefined gene signatures. Spearman correlation analysis was used to examine the associations between aDC abundance and functional scores. Samples were divided into aDC-high and aDC-low groups according to the median aDC proportion.

T cell subclustering and composition analysis

T cells were extracted and reclustered according to canonical marker genes. $CD8^+$ T cells were classified into naïve, memory, effector, and exhausted populations, whereas $CD4^+$ T cells

were classified into naïve, memory, T follicular helper, atypical, and regulatory T cell populations. The relative abundance of each T cell subset was calculated for individual samples and compared between the aDC-high and aDC-low groups.

Cell-cell communication analysis

Cell-cell communication between DC and T cell subsets was inferred using the CellChat R package. CCL, CD80, and MHC-I signaling networks were further examined, based on MHC-I-CD8, CD80/CD86-CD28, and CCL19-CCR7 ligand-receptor interactions.

Association with T cell effector activity

DC functional scores were calculated as described above, and $CD8^+$ T cell abundance was quantified based on the relative proportion of $CD8^+$ T cells. Cytotoxic effector activity was assessed based on the expression of NKG7, GZMA, and GZMK. Spearman rank correlation analysis was then performed to evaluate the associations of DC functional scores with $CD8^+$ T cell abundance and cytotoxic effector activity.

Validation in an independent cohort

An independent scRNA-seq cohort was analyzed using the same analytical workflow. DC subsets were annotated according to the same marker-based criteria. The associations of aDC abundance with DC maturation, MHC-I antigen presentation, cGAS-STING signaling, and oxidative stress were independently reassessed.

Synthesis of IrMn-OVA@aDCM NAs

IrMn nanoparticles were synthesized via a one-pot hydrothermal method. Briefly, $MnCl_2$ (2 mM) and $IrCl_3$ (1 mM) were dispersed in 20 mL of 10 mM NaOH aqueous solution containing 80 mg of polyvinylpyrrolidone (PVP). The mixture was stirred at room temperature for 30 min and subsequently heated at 80°C for 10 h in a water bath. After synthesis, the products were purified by dialysis against deionized water for 24 h and subsequently freeze-dried to obtain IrMn nanoparticles. For OVA loading, IrMn nanoparticles were dispersed in water at a concentration of 2 mg/mL (5 mL), followed by the addition of 30 mg ovalbumin (OVA). The

mixture was stirred at 37°C overnight to facilitate OVA adsorption onto IrMn nanoparticles, yielding IrMn-OVA.

To generate activated DC membrane, DC2.4 cells were stimulated with MC38 tumor cell culture supernatant for 24 h. The stimulated cells were collected, and cell membranes were isolated using a standard membrane extraction protocol. The protein concentration of the extracted cell membrane was quantified using a bicinchoninic acid (BCA) protein assay.

IMOD NAs was prepared by co-extrusion of IrMn-OVA (IMO) and activated DC membrane (aDCM) at a mass ratio of 1:1 using a mini extruder equipped with 100 nm polycarbonate membranes. The resulting membrane-coated nanoparticles were further purified by dialysis for 24 h and subsequently freeze-dried for storage.

Characterization of nanoadjuvants

The morphology and particle size of IM, IMO, and IMOD NAs were observed by transmission electron microscopy (TEM; Tecnai G2 F20, FEI). The hydrodynamic size and zeta potential of the nanoparticles were measured using a Zetasizer Nano ZS90 (Malvern). The elemental composition of IMOD NAs was analyzed by energy-dispersive X-ray spectroscopy (EDS; Tecnai G2 F30, FEI). X-ray photoelectron spectroscopy (XPS; ESCALAB 250Xi, Thermo Fisher Scientific) was used to analyze the elemental composition and valence states of the nano-adjuvants. ESR spectra was acquired on the Bruker EMX1598 spectrometer. The contents of Mn and Ir were determined by inductively coupled plasma mass spectrometry (ICP-MS; PlasmaQuant MS, Analytik Jena).

Cell lines and culture

The murine colon carcinoma cell line MC38 was obtained from the Cell Bank of the Chinese Academy of Sciences (Shanghai, China), and the murine dendritic cell line DC2.4 was purchased from Sunncell (Wuhan, China). MC38 cells were cultured in high-glucose Dulbecco's modified Eagle's medium (DMEM) supplemented with 10% fetal bovine serum (FBS) and 1% penicillin-streptomycin. DC2.4 cells were maintained in RPMI-1640 medium

supplemented with 5% FBS and 1% penicillin-streptomycin. All cells were cultured at 37°C in a humidified incubator with 5% CO_2.

Cell viability assay

Cell viability was assessed using a Cell Counting Kit-8 (CCK-8; C0037, Beyotime). DC2.4 and NIH-3T3 cells were separately seeded in 96-well plates and assigned to four treatment groups: control, IM, IMO, and IMOD NAs. Following 24 h of treatment, CCK-8 reagent was added to each well, and the cells were incubated at 37°C for an additional 1 h. Absorbance at 450 nm was subsequently measured using a Cytation 5 multimode microplate reader (BioTek). Cell viability was expressed as a percentage relative to that of the untreated control group.

Cellular uptake and DC-targeting evaluation

To evaluate the cellular uptake and preferential uptake of IMOD NAs by DCs, DC2.4 and NIH-3T3 cells were separately seeded in 24-well plates at a density of 2×10^4 cells per well and incubated with IMOD NAs containing FITC-labeled OVA (FITC-OVA) for 1, 2, or 4 h at 37°C. At the indicated time points, cells were washed three times with phosphate-buffered saline (PBS) to remove extracellular nano-adjuvants and subsequently fixed with 4% paraformaldehyde. Nuclei were counterstained with DAPI for 3 min. Fluorescence images were acquired using a confocal laser-scanning microscope, and fluorescence intensity profiles were further analyzed by line-scan analysis using Image J. The cellular uptake of IMOD NAs was compared between DC2.4 and NIH-3T3 cells based on the intracellular FITC-OVA fluorescence signal.

To investigate the effect of DC membrane coating on the cellular uptake of nano-adjuvants, DC2.4 cells were incubated with IMO or IMOD NAs containing FITC-labeled OVA (FITC-OVA). Following incubation, cells were thoroughly washed with PBS to remove extracellular nanoadjuvants and subsequently analyzed by flow cytometry. Cellular uptake was quantified based on the FITC fluorescence intensity, allowing comparison of the uptake efficiency of IMO and IMOD NAs by DC2.4 cells.

Intracellular trafficking and lysosomal escape

DC2.4 cells were seeded in 24-well plates at a density of 2×10^4 cells per well and allowed to adhere for 24 h. Cells were subsequently incubated with IMOD NAs containing FITC-labeled OVA (FITC-OVA) for the indicated time periods. At each time point, lysosomes were stained with LysoTracker Red to visualize lysosomal compartments. Fluorescence images were acquired using confocal laser-scanning microscopy (CLSM). The intracellular trafficking and lysosomal escape of OVA were evaluated based on the time-dependent spatial relationship between FITC-OVA and LysoTracker Red fluorescence signals, with reduced colocalization indicating the release of OVA from lysosomal compartments.

T cell-mediated tumor cell killing assay

The tumor-killing activity of $CD8^+$ T cells following DC-mediated antigen presentation was evaluated using a Calcein-AM/propidium iodide (PI) Live/Dead Cell Staining Kit (C1371S, Beyotime). DC2.4 cells were first stimulated with the indicated nano-adjuvant formulations to induce DC activation and were subsequently co-cultured with $CD8^+$ T cells for antigen presentation and T cell activation. The activated $CD8^+$ T cells were then collected and co-cultured with MC38-OVA tumor cells seeded in 96-well plates. After 24 h of co-culture, the culture medium was removed and replaced with fresh medium containing Calcein-AM and PI. Following incubation for 30 min, fluorescence images were acquired using a fluorescence microscope. Viable tumor cells were identified by green Calcein-AM fluorescence, whereas dead cells exhibited red PI fluorescence. The cytotoxic activity of $CD8^+$ T cells against MC38-OVA cells was evaluated based on the extent of tumor cell death.

Intracellular ROS detection

Intracellular reactive oxygen species (ROS) levels in DC2.4 cells were measured using a ROS Assay Kit (S0033S, Beyotime). DC2.4 cells were seeded in 6-well plates and assigned to five treatment groups: control, OVA, IM, IMO, and IMOD NAs. Following the indicated treatments, cells were harvested and incubated with 10 μM 2′,7′-dichlorodihydrofluorescein

diacetate (DCFH-DA) at 37°C for 30 min. Cells were subsequently washed three times with PBS to remove excess probe. Intracellular ROS levels were quantified by flow cytometry (FACSCelesta, BD Biosciences) based on DCF fluorescence intensity.

RNA sequencing and differential expression analysis

Total RNA was extracted from DC2.4 cells according to the manufacturer's instructions. RNA sequencing (RNA-seq) was performed by Novogene. Differentially expressed genes (DEGs) were identified using a significance threshold of $P < 0.05$ and $|\log2(\text{fold change})| > 0$. Functional enrichment analysis of DEGs was performed using the clusterProfiler package in R.

Western blotting

Total proteins were extracted from $CD8^+$ T cells or DC2.4 cells using RIPA lysis buffer (P0013C, Beyotime) supplemented with 1% phenylmethylsulfonyl fluoride (PMSF; HY-B0496, MCE), 1% protease inhibitor cocktail (HY-K0010, MCE), and 1% phosphatase inhibitor cocktail (HY-K0022, MCE). Cell lysates were centrifuged at 10,000 g for 25 min at 4°C, and the resulting supernatants were collected. Protein concentrations were determined using a BCA Protein Assay Kit (P0009, Beyotime) according to the manufacturer's instructions. Protein samples were mixed with 5×SDS-PAGE sample loading buffer under reducing conditions and denatured at 95°C for 5 min. Equal amounts of protein were separated by SDS-PAGE and subsequently transferred onto polyvinylidene fluoride (PVDF) membranes (IPVH00010, Merck Millipore).

The membranes were incubated with the following primary antibodies at the indicated dilutions: CCR7 (1:1000, BS47171, Bioworld), granzyme B (GZMB; 1:1000, YP-mAb-10805, UpingBio), perforin (1:1000, YP-mAb-10607, UpingBio), GAPDH (1:5000, M20006, Abmart), NF-κB p65 (1:1000, R012746, Epizyme), phospho-NF-κB p65 (p-NF-κB p65; 1:1000, R013789, Epizyme), phospho-TBK1 (p-TBK1; 1:1000, PC3440, Abmart), phospho-STING (p-STING; 1:1000, BS79500, Bioworld), phospho-IRF3 (p-IRF3; 1:1000, PC3195, Abmart), STING (1:1000, BS80431, Bioworld), and β-actin (1:3000, AF7018, Affinity). After incubation

with the appropriate horseradish peroxidase (HRP)-conjugated secondary antibodies for 1 h, protein bands were visualized using a chemiluminescence imaging system (Tanon 5200).

Intracellular GSH measurement

DC2.4 cells were seeded in 12-well plates and treated with different nanoadjuvant for 24 h. Cells were then lysed by three freeze–thaw cycles, followed by centrifugation at 10,000 *g* for 10 min at 4°C. The intracellular glutathione (GSH) level in the resulting supernatant was determined using Ellman's assay.

Immunofluorescence and multiplex immunofluorescence staining

For immunofluorescence staining of DC2.4 cells, cells were fixed in 4% paraformaldehyde for 30 min on ice following the indicated treatments and subsequently permeabilized with 0.2% Triton X-100 for 30 min. After blocking with 5% bovine serum albumin (BSA) for 1 h, cells were incubated overnight at 4°C with an anti-CCR7 antibody (1:200, BS47171, Bioworld), followed by incubation with an appropriate fluorescently labeled secondary antibody. For F-actin staining, cells were incubated with Phalloidin-iFluor 594 reagent (1:200, ab176757, Abcam). Nuclei were counterstained with DAPI (C0060, Solarbio).

For immunofluorescence staining of mouse tumor tissues, paraffin-embedded sections were deparaffinized and subjected to antigen retrieval in sodium citrate buffer. Sections were then permeabilized with 0.2% Triton X-100 and blocked with 5% BSA. Subsequently, sections were incubated overnight at 4°C with primary antibodies against CD8 (1:200, GB15068, Servicebio) or granzyme B (GZMB; 1:200, GB150173, Servicebio), followed by incubation with appropriate fluorescently labeled secondary antibodies. Nuclei were counterstained with DAPI.

For multiplex immunofluorescence (mIF) staining of mouse lymph node tissues, paraffin-embedded sections were subjected to six-marker, seven-color multiplex immunofluorescence staining using a tyramide signal amplification (TSA)-based Opal multiplex immunofluorescence system. Sequential staining was performed for CD11c, MHC-I, CD86, CD8, GZMB, and forkhead box P3 (FOXP3), with individual targets detected in successive

staining cycles using the corresponding primary antibodies and Opal fluorophores. Hoechst was used for nuclear counterstaining. The stained sections were subsequently subjected to multispectral fluorescence imaging for visualization and analysis of the spatial distribution and phenotypic characteristics of the indicated immune cell populations.

Fluorescence images were acquired using a confocal laser-scanning microscope unless otherwise indicated.

IFN-γ ELISpot assay

DC2.4 cells were treated with different nanoadjuvants for the indicated period and subsequently washed to remove residual materials. The treated DC2.4 cells were then co-cultured with $CD8^+$ T cells at the indicated ratio. IFN-γ secretion by $CD8^+$ T cells was evaluated using a mouse IFN-γ ELISpot kit (SinoBiological, EK50709B) according to the manufacturer's instructions. Briefly, DC2.4 cells and $CD8^+$ T cells were seeded into IFN-γ antibody-precoated ELISpot plates and co-cultured under the indicated conditions. After incubation, the cells were removed, and captured IFN-γ was detected using the corresponding biotinylated detection antibody, enzyme conjugate, and substrate solution. Spot-forming units (SFUs) were imaged and quantified using an automated ELISpot reader. The number of IFN-γ positive spots was used to evaluate the ability of nano-adjuvant-treated DC2.4 cells to stimulate $CD8^+$ T cell effector responses.

Immunohistochemical staining

Paraffin-embedded mouse lymph node sections were deparaffinized, subjected to antigen retrieval, and permeabilized as described above for immunofluorescence staining. Endogenous peroxidase activity was quenched by incubation with 3% H_2O_2 for 25 min, followed by blocking with 5% bovine serum albumin (BSA) for 30 min. Sections were then incubated overnight at 4°C with primary antibodies against CD8 (1:400, GB15068, Servicebio) or Ki67 (1:1,000, GB111499, Servicebio). The following day, sections were incubated with a biotinylated anti-rabbit IgG secondary antibody for 2 h at room temperature. Immunoreactivity was visualized

using 3,3′-diaminobenzidine (DAB), followed by hematoxylin counterstaining. Sections were subsequently dehydrated through a graded ethanol series and imaged using a light microscope (ECLIPSE Ci-L, Nikon).

***In vivo* biodistribution and draining lymph node uptake**

To investigate the *in vivo* biodistribution of the nanoadjuvants, Cy5.5-labeled IMO and IMOD NAs were administered to mice by footpad injection at a dose of 20 mg/kg in a total volume of 100 μL. Fluorescence images were acquired at the indicated time points after injection using an *in vivo* imaging system (IVIS; ABL X5, Tanon). At the selected time points, the draining lymph nodes and main organs (hearts, livers, spleens, lungs, and kidneys) were collected for *ex vivo* fluorescence imaging to evaluate the tissue distribution and lymph node accumulation of IMO and IMOD NAs.

Based on the fluorescence imaging results, 12 h after injection was selected as the time point of maximal accumulation in the draining lymph nodes. The draining lymph nodes were then harvested and processed into single-cell suspensions. Cells were stained with an anti-CD11c antibody and analyzed by flow cytometry. The proportion of $CD11c^{+}Cy5.5^{+}$ cells were quantified to compare the uptake of IMO and IMOD NAs by DCs in the draining lymph nodes.

Animals and tumor models

Female C57 mice (6 weeks old, 18-22 g) were purchased from Beijing HFK Bio-Technology Co., Ltd. Mice were housed under standard specific-pathogen-free conditions at 23 ± 2°C and 40-70% relative humidity under a 12 h light/12 h dark cycle, with free access to food and water.

To establish the tumor-bearing mouse model, luciferase-expressing MC38-OVA cells (MC38-OVA-Luc; 1×10^{6} cells per mouse) were injected into the right inguinal region of each mouse. Tumor establishment and progression were longitudinally monitored by bioluminescence imaging using an *in vivo* imaging system (IVIS; ABL X5, Tanon). Bioluminescence images were acquired and quantitatively analyzed to assess tumor growth.

All animal experiments were conducted in accordance with the Laboratory Animals

Guideline for Ethical Review of Animal Welfare and were approved by the Ethics Committee for Medical Laboratory Animals of China Medical University (approval no. CMU20260385).

***In vivo* combination therapy with αPD-L1**

Eight days after inoculation with MC38-OVA-Luc cells, tumor-bearing mice were randomly assigned to five treatment groups: (a) PBS, (b) IMO, (c) IMOD, (d) IMO plus αPD-L1, and (e) IMOD plus αPD-L1. Mice in the PBS group received 100 μL PBS, whereas mice in the IMO and IMOD groups received 100 μL of the corresponding nano-adjuvant formulation (2 mg/mL). Beginning on day 9 after tumor inoculation, nano-adjuvants were administered every other day on days 9, 11, 13, 15, 17, and 19, for a total of six doses. In the combination-treatment groups, αPD-L1 was administered intraperitoneally at a dose of 100 μg per mouse in a total volume of 100 μL on days 10, 14, and 18, for a total of three doses. Thus, αPD-L1 administration was intercalated between successive nanoadjuvant treatments to establish an alternating "sandwich" combination-treatment regimen.

Body weight and tumor growth were monitored throughout the treatment period, and survival was recorded thereafter. Tumor dimensions were measured periodically, and tumor volume was calculated using the formula $V = \text{length} \times \text{width}^2/2$. Tumor progression was additionally monitored by longitudinal bioluminescence imaging using an in vivo imaging system (IVIS; ABL X5, Tanon). On day 22, mice designated for endpoint analysis were euthanized, and tumors were harvested for histopathological evaluation, including hematoxylin and eosin (H&E) staining, terminal deoxynucleotidyl transferase dUTP nick-end labeling (TUNEL), and Ki67 immunostaining.

Assessment of antitumor immune responses

Lymph nodes were harvested from the indicated mice and processed to obtain single-cell suspensions. For T cell phenotyping, cells were stained with fluorophore-conjugated antibodies against CD45 (PerCP/Cyanine5.5), CD3 (Elab Fluor® Violet 450), CD4 (Elab Fluor® Red 780), and CD8a (PE/Cyanine7) for 30 min. Following surface staining, cells were fixed and

permeabilized and subsequently stained intracellularly with an anti-Foxp3 antibody (Elab Fluor® 700). Samples were analyzed by flow cytometry (FACSCelesta, BD Biosciences) to determine the frequencies of $CD4^+$ T cells, $CD8^+$ T cells, and $CD4^+Foxp3^+$ regulatory T cells (Tregs).

For DC analysis, lymph node single-cell suspensions were stained for 30 min with fluorophore-conjugated antibodies against CD11c (FITC), CD86 (PE), CD80 (APC), and CCR7 (BV421). Samples were subsequently analyzed by flow cytometry to assess DC activation and maturation based on the expression of CD80, CD86, and CCR7 within the $CD11c^+$ cell population.

***In Vivo* Biocompatibility Evaluation.**

Female C57 mice (6 weeks old, 18-22 g) were randomly assigned to three groups (n = 5 per group) and intravenously administered PBS, IMO, or IMOD NAs, respectively. Hematological parameters, including red blood cell (RBC) count, white blood cell (WBC) count, hemoglobin (HGB), and platelet (PLT) count, were analyzed. Serum biochemical parameters, including alanine aminotransferase (ALT), aspartate aminotransferase (AST), blood urea nitrogen (BUN), and creatinine (CRE), were also measured to evaluate potential systemic toxicity. In addition, the heart, liver, spleen, lung and kidney were harvested, fixed in 10% neutral buffered formalin, embedded in paraffin, sectioned, and stained with hematoxylin and eosin (H&E) for histopathological examination.

Statistical analysis

All experiments and data analyses were performed in a blinded manner. Unless otherwise stated, experiments were independently repeated at least three times. Quantitative data are presented as the mean ± SEM. Comparisons between two groups were performed using Student's t-test, whereas comparisons among multiple groups were performed using one-way ANOVA. Image quantification was performed using Image J. Bioinformatic and statistical analyses of single-cell RNA sequencing (scRNA-seq) and bulk RNA sequencing (bulk RNA-

seq) data were performed using R (version 4.2.3) and Python (version 3.7.16). Statistical analyses and graphical presentation of other experimental data were performed using GraphPad Prism 8 and Origin 2018. All statistical tests were two-sided unless otherwise specified, and *P*-values < 0.05 was considered statistically significant. Statistical significance is indicated as follows: * $P < 0.05$, ** $P < 0.01$ and *** $P < 0.001$.

2. Results

3.1. scRNA-seq and bulk RNA-seq revealed heterogeneity of DC subsets in LNs.

To define the cellular landscape of tumor-draining lymph nodes (TDLNs) in colon cancer, we integrated single-cell RNA-sequencing data from eight patients. Following integration, cells segregated primarily by lineage, resolving diverse T cell, B cell, myeloid, and stromal populations (Figure S1, A-C). These populations included multiple $CD4^+$ and $CD8^+$ T cell states, natural killer cells, B cells, monocytes and macrophages, dendritic cells (DCs), neutrophils, and fibroblasts. T and B cells dominated the lymphoid compartment, whereas DCs and other myeloid populations occupied transcriptionally distinct regions, highlighting the cellular complexity of both adaptive and innate immunity within TDLNs (**Figure** 1A).

Canonical marker expression supported the annotation of the major immune and stromal populations. Activated DCs were characterized by LAMP3 and FSCN1, conventional DCs by CLEC10A and CD1C, and plasmacytoid DCs by LILRA4 and IL3RA (Figure S1D). Reclustering of the DC compartment identified four distinct subsets, including $IDO1^+$ cDC1, $LAMP3^+$ activated DCs (aDCs), $CLEC10A^+$ cDC2, and $LILRA4^+$ pDCs. (Figure 1B). Among these subsets, LAMP3 and the costimulatory molecule CD80 were selectively enriched in aDCs and expressed at markedly higher levels than in the other DC populations (Figure 1C). aDCs also exhibited the highest MHC-I and lymphocyte costimulation scores, consistent with an enhanced capacity for antigen presentation and T cell costimulation (Figure 1D and Figure S1E).

We next examined whether aDC abundance was associated with tissue-level immune programs across TDLN samples. The proportion of aDCs correlated positively with cGAS-STING pathway activity ($R = 0.56$, $P = 8.6 \times 10^{-4}$) and oxidative stress activity ($R = 0.47$, $P = 0.0068$), linking aDC accumulation to heightened innate immune sensing and oxidative stress within the lymph node (Figure 1E). Genes enriched in aDCs mapped to TNF-NF-κB, interferon-γ, Toll-like receptor, and CD40 signaling pathways, together with programs involved in lymphocyte activation, T cell activation, and adaptive immune regulation(Figure 1F).

Consistent with these pathway-level associations, aDCs expressed higher levels of the CGAS-STING components TMEM173, TBK1, and IRF3, as well as oxidative stress-response genes, including TXN, TNFAIP3, and GPX4 (Figure 1G). Together, these findings define LAMP3^{+} aDCs as an inflammatory and immunostimulatory DC state associated with STING-related innate immune activation and oxidative stress adaptation in colon cancer TDLNs (Figure S1F).

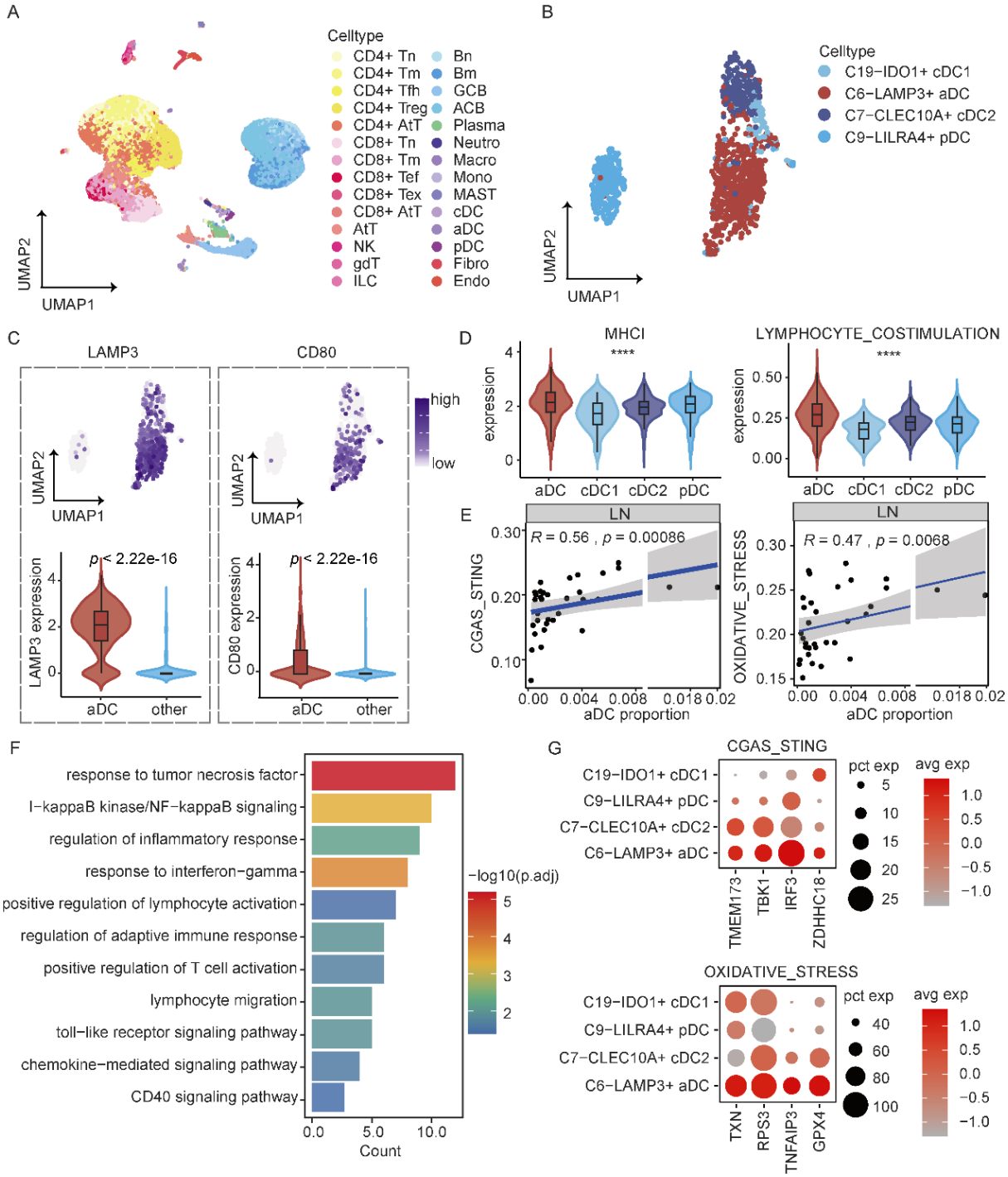


Figure 1. The functional and state heterogeneity in DC subsets of LNs. (A) UMAP of major

lymph node cell populations. (B) UMAP of DC subsets. (C) UMAP feature plots showing the expression of the aDC-associated marker LAMP3 and the costimulatory molecule CD80. Violin plots compare LAMP3 and CD80 expression between aDCs and other cells, showing significantly higher expression in aDCs. (D) MHC-I and lymphocyte costimulation pathway scores across DC subsets. (E) Correlations of aDC abundance with cGAS-STING and oxidative stress pathway activity. (F) Gene Ontology enrichment analysis of aDC-enriched genes. (G) Expression of cGAS-STING and oxidative stress-related genes across DC subsets.

3.2. The aDC immunostimulatory state is a key to immune activation in LNs.

We then profiled the T cell compartment in relation to the LAMP3$^+$ activated dendritic cell (aDC) state in tumor-draining lymph nodes (TDLNs). Reclustering resolved CD8$^+$ T cells into naïve, memory, effector, exhausted, and atpical populations. CD4$^+$ T cells comprised naïve, memory, atpical, follicular helper, and regulatory populations (**Figure** 2A and 2B). Canonical marker expression supported these assignments (Figure S2A). Samples were first stratified by median aDC abundance. aDC-high samples contained more CD8$^+$ effector T cells and fewer CD8$^+$ naïve T cells than aDC-low samples (Figure 2C). Thus, aDC enrichment was associated with a shift toward a more differentiated CD8$^+$ T cell compartment.

Innate sensing and antigen-presentation programs varied markedly across individual TDLNs. cGAS-STING, oxidative stress, costimulation, and MHC-I signature scores showed coordinated changes across samples (Figure 2D). Hierarchical clustering based on these signatures separated the samples into pathway-high and pathway-low groups. The pathway-high group contained fewer naïve CD4$^+$ and CD8$^+$ T cells. It also showed increased proportions of CD4$^+$ follicular helper T cells and CD8$^+$ effector T cells (Figure 2E and Figure S2B). These findings associated coordinated activation of innate immune and antigen-presentation programs with a shift away from naïve T cell states and toward antigen-experienced populations.

We then assessed potential communication between DC and CD8$^+$ T cell subsets. Ligand-receptor analysis predicted extensive interactions between aDCs, cDC1s, and cDC2s and naïve,

memory, effector, and exhausted $CD8^+$ T cells. Although all three DC subsets were connected to each $CD8^+$ T cell state, aDCs displayed the broadest inferred interaction profile (Figure 2F). Prominent signaling pairs included CCL19-CCR7, CD80/CD86-CD28, and HLA class I-CD8A/CD8B (Figure 2G). These interactions were consistent with chemotactic recruitment, costimulation, and MHC-I dependent T cell engagement. Network centrality analysis further identified aDCs as major sources of outgoing CCL and CD80 signals (Figure S2C). Bulk tissue transcriptomic analysis supported these single-cell findings. cGAS-STING and costimulation scores correlated positively with $CD8^+$ T cell signatures. They also correlated with NKG7, GZMA, and GZMK expression (Figure S2D). Together, these data place $LAMP3^+$ aDCs within an immune program marked by innate sensing, antigen presentation, and costimulation. This program is associated with the accumulation of antigen-experienced T cell populations in colon cancer TDLNs.

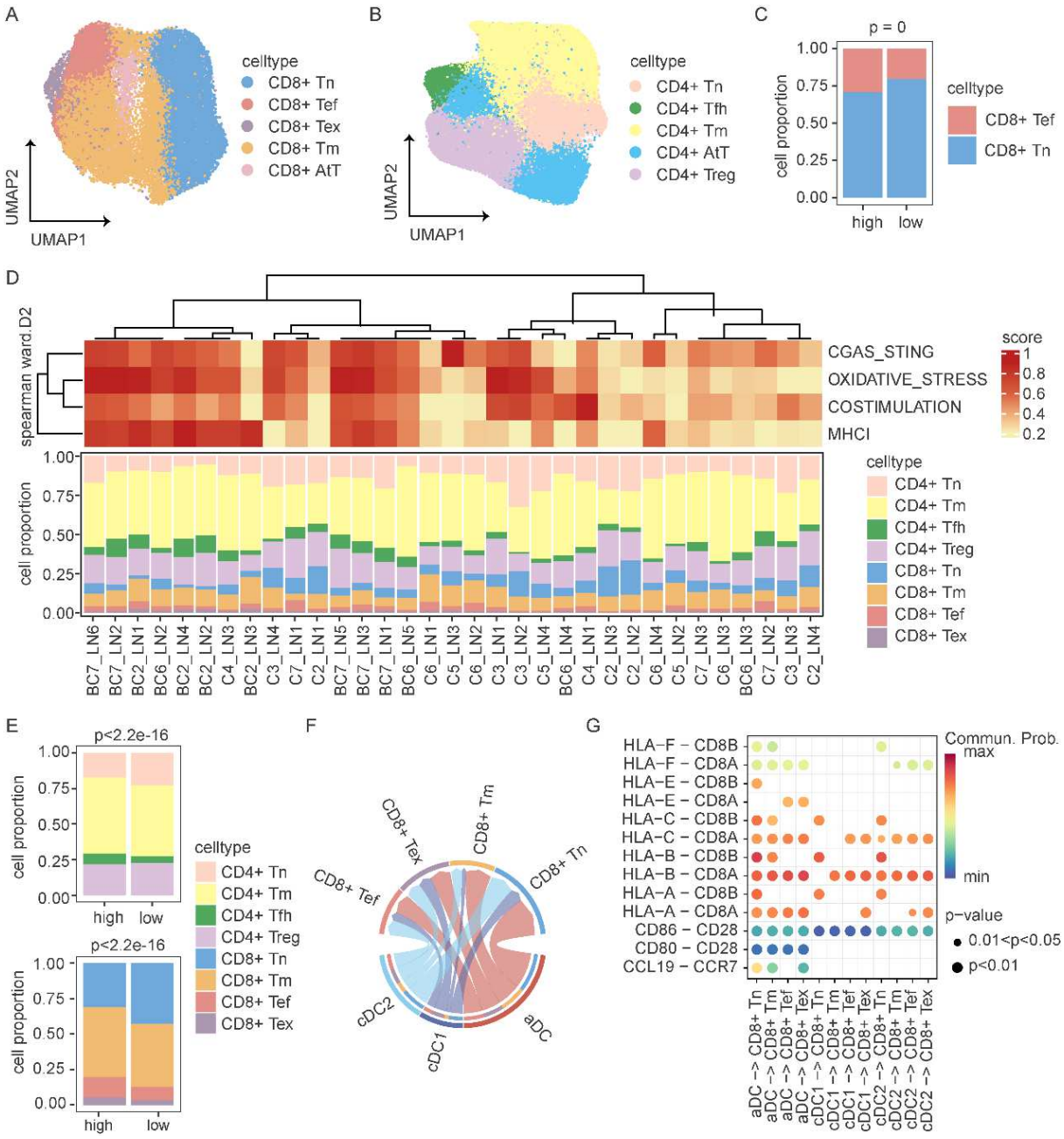


Figure 2. T cell subset composition and DC-T cell communication in lymph nodes. (A and B) UMAP visualization of CD8⁺ (A) and CD4⁺ (B) T cell subsets. (C) Relative frequencies of CD8⁺ naïve T cells (Tn) and effector T cells (Tef) in samples stratified by median aDC abundance. (D) Hierarchical clustering of lymph node samples based on cGAS-STING, oxidative stress, costimulation, and MHC-I signature scores, with the corresponding T cell composition shown below. (E) T cell subset composition in the high- and low-score groups defined in (D). (F) Inferred communication between aDC, cDC1, and cDC2 subsets and CD8⁺ T cell states. (G) Selected ligand-receptor interactions mediating DC-CD8⁺ T cell

communication, including CCL19-CCR7, CD80/CD86-CD28, and HLA class I-CD8A/CD8B axes.

3.3. Characterization and properties of IMOD NAs

The morphology and physicochemical properties of IMOD NAs were first characterized. TEM images showed that IM nanoparticles were well dispersed with a relatively uniform morphology, while the clear Tyndall effect of the aqueous suspension indicated good colloidal dispersion (**Figure** 3A). HRTEM revealed distinct lattice fringes with a spacing of 0.18 nm (Figure 3B). According to the TEM images, the average particle size of IM was 12.65 ± 2.50 nm (Figure 3C). After cell membrane coating, a clear shell layer could be observed around the nanoparticle core, giving IMOD NAs a typical core-shell structure (Figure 3D). HAADF-STEM imaging and elemental mapping showed that Mn, Ir, and O were uniformly distributed throughout the nanoparticles (Figure 3E). All the expected elemental signals were identified in the X-ray photoelectron spectroscopy (XPS) spectra (Figure S3), providing further evidence for the successful construction of the IMOD NAs. More specifically, XPS was used to examine the chemical states of Ir and Mn. The high-resolution Ir 4f spectrum showed the presence of Ir^0, Ir^{3+}, and Ir^{4+} species, whereas the Mn 2p spectrum indicated the coexistence of Mn^{2+} and Mn^{4+} (Figure 3F, G). Protein analysis showed that the characteristic OVA and membrane protein bands were retained in IMOD NAs, supporting the incorporation of OVA and the membrane coating (Figure 3H). Consistent with these results, the hydrodynamic diameter increased after OVA loading and membrane modification, together with changes in ζ potential (Figure 3I).

The redox properties of IMOD NAs were subsequently examined. In the presence of H_2O_2, IMOD NAs produced a marked ESR signal, whereas only a weak signal was detected in the absence of H_2O_2 (Figure 3J), indicating H_2O_2-dependent radical generation. IMOD NAs also caused a progressive decrease in GSH content with increasing incubation time, while little change was observed in the PBS control (Figure 3K). In parallel, the GSSG level increased after

incubation with IMOD NAs (Figure 3L), suggesting that GSH was continuously oxidized during the reaction. These results show that IMOD NAs can consume GSH and alter the local redox environment. The release behavior of Mn^{2+} was further evaluated at different pH values. IMOD NAs released Mn^{2+} more rapidly at pH 5.0 than at pH 7.4, with a substantially higher cumulative release under acidic conditions (Figure 3M). This pH-dependent release behavior favors Mn^{2+} liberation in acidic intracellular compartments such as lysosomes.

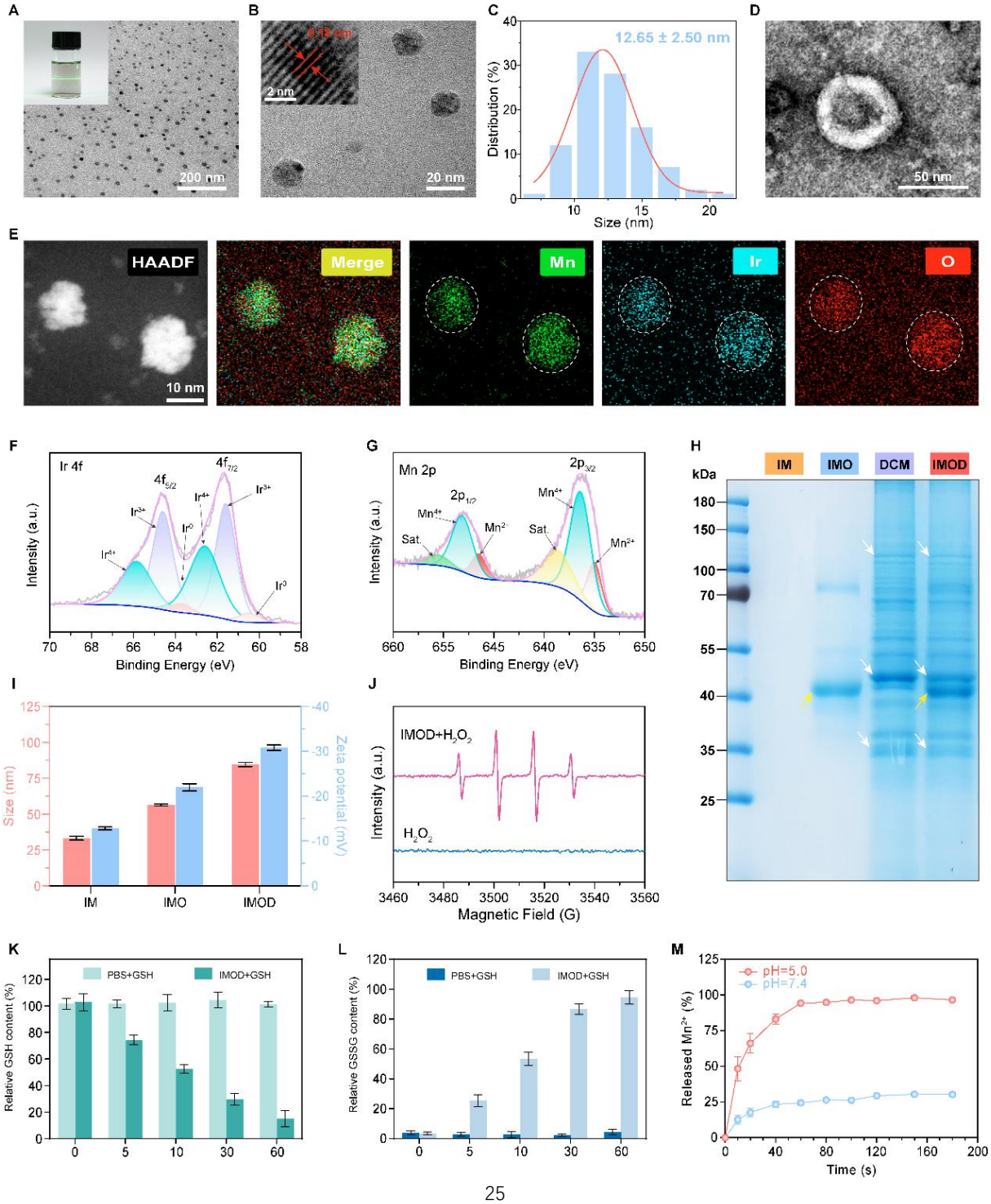


Figure 3. Physicochemical characterization and redox properties of IMOD NAs. (A) TEM image of IM; inset: Tyndall effect of the IM dispersion. (B) HRTEM image of IM; inset: lattice fringes with a d-spacing of 0.18 nm. (C) Size distribution of IM (12.65 ± 2.50 nm). (D) TEM image of membrane-coated IMOD NAs showing a core-shell structure. (E) HAADF-STEM image and elemental mappings of Mn, Ir, and O in IM. (f,g) High-resolution XPS spectra of Ir 4f (F) and Mn 2p (G). (H) Protein analysis of IM, IMO, DCM, and IMOD NAs for verification of OVA loading and membrane coating. (I) Hydrodynamic size and ζ-potential of IM, IMO, and IMOD NAs. (J) ESR spectra of IMOD NAs in the absence or presence of H_2O_2. (K, L) Relative GSH content (K) and GSSG content (L) after incubation with PBS or IMOD NAs. (M) Mn^{2+} release from IMOD NAs at pH 5.0 and 7.4. $n = 3$.

3.4. IMOD NAs drives DCs maturation through coordinated NF-κB and STING activation

The effects of IMOD NAs on DCs were first evaluated *in vitro*. IMOD NAs showed low cytotoxicity across the tested concentration range (**Figure** 4A). It also promoted DC2.4 cell proliferation during prolonged incubation. This effect was greater than that induced by IMO (Figure 4B). The DC membrane coating enhanced the cellular uptake of IMOD NAs. FITC-labeled IMOD NAs accumulated rapidly in DC2.4 cells but showed limited uptake by NIH-3T3 fibroblasts (Figure 4C). Thus, the homologous membrane coating conferred preferential recognition and internalization by DCs. IMOD NAs initially colocalized with lysosomes after cellular entry. This colocalization progressively decreased over time (Figure 4D), indicating efficient lysosomal escape. This process facilitated cytosolic OVA release and protected the antigen from lysosomal degradation. Flow cytometry further showed that IMOD NAs was internalized more rapidly and efficiently than the uncoated IMO formulation (Figure 4E).

Mechanistically, IMOD NAs was designed to activate two complementary innate immune signaling pathways (Figure 4F). It promoted intracellular glutathione depletion and disrupted redox homeostasis. This response led to robust ROS accumulation in DC2.4 cells (Figure 4G)

and subsequent activation of NF-κB signaling. In parallel, Mn^{2+} released from IMOD NAs activated the STING-TBK1-IRF3 axis. These two signals converged to promote DC maturation. Bulk RNA sequencing supported this mechanism. IMOD NAs increased the activity of the NF-κB, costimulatory, and cGAS-STING pathways (Figure 4H). It also up-regulated genes associated with DC activation and innate immune signaling, including Cd83, Cd40, Tlr3, and Ifnb1 (Figure 4I-J). The induced genes were enriched in oxidative stress responses, immune-cell activation, chemotaxis, T cell activation, and antigen processing and presentation (Figure 4K). Gene set enrichment analysis (GSEA) showing significant enrichment of pathways related to cell chemotaxis, lymphocyte-mediated signaling, NF-κB signaling, inflammatory regulation, response to tumor necrosis factor, and Toll-like receptor signaling (Figure S4). These transcriptional changes indicated broad enhancement of the antigen-presenting and immunostimulatory functions of DCs.

Western blotting confirmed activation of both pathways. IMOD NAs increased NF-κB phosphorylation (Figure 4L). It also enhanced the phosphorylation of STING, TBK1, and IRF3 (Figure 4M). These changes were accompanied by increased IFN-β secretion (Figure 4N). Inhibition of either NF-κB or STING markedly impaired IMOD-induced DC maturation (Figure 4O). Together, these results show that DC membrane-coated IMOD NAs undergoes rapid homotypic uptake and lysosomal escape. It then promotes antigen release and drives DC maturation through coordinated ROS-NF-κB and Mn^{2+}-STING signaling.

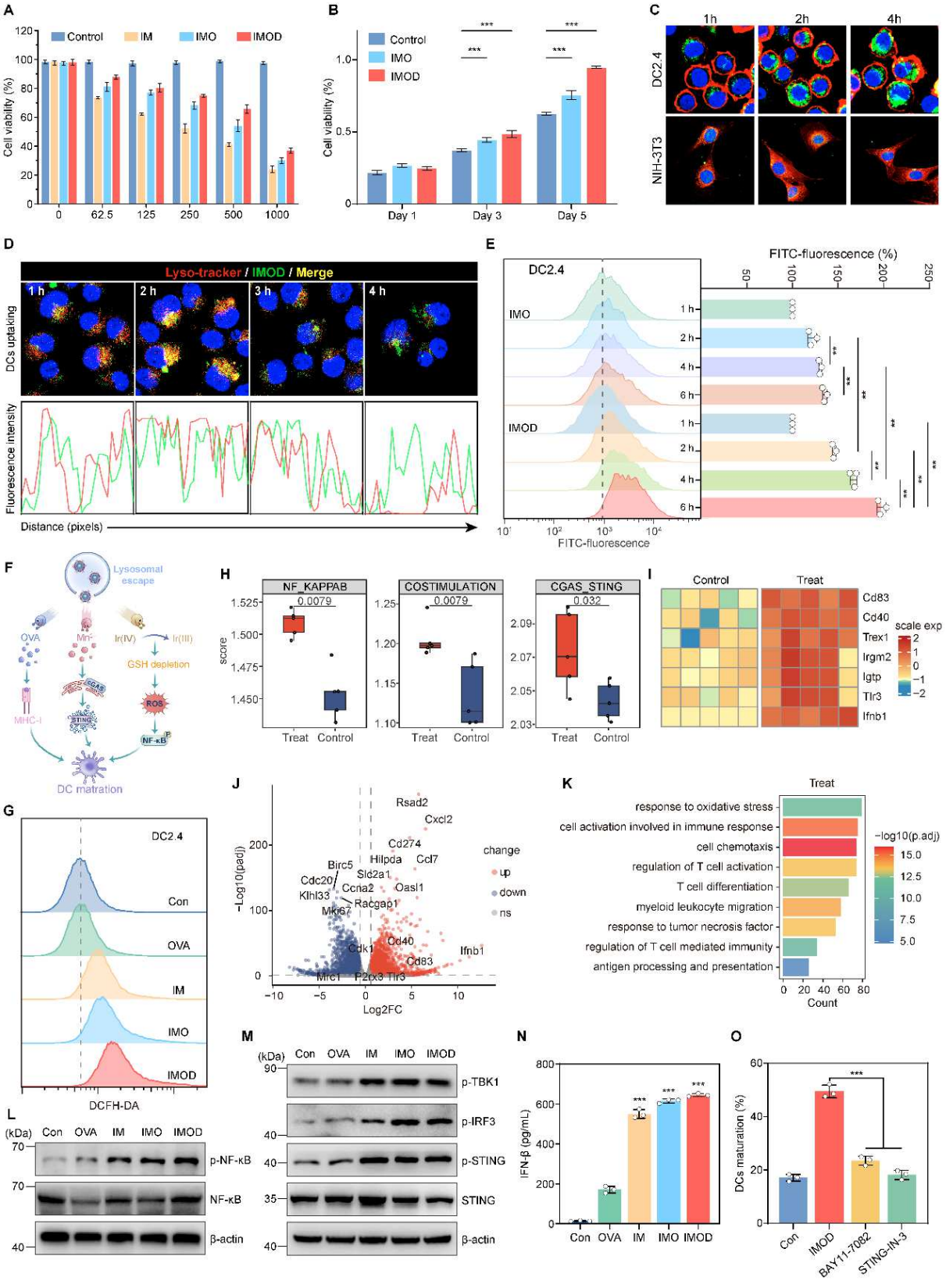


Figure 4. Mechanisms underlying IMOD NAs induced DCs maturation. (A) CCK-8 assay of DC2.4 cell viability after treatment with IM, IMO, or IMOD NAs. (B) Proliferation of DC2.4 cells incubated with IMO or IMOD NAs. (C) Time-dependent uptake of FITC-labeled IMOD

by DC2.4 and NIH-3T3 cells. (D) Colocalization of FITC-labeled IMOD with lysosomes in DC2.4 cells and corresponding fluorescence intensity profiles. (E) Flow cytometric analysis of IMO and IMOD NAs uptake by DC2.4 cells. (F) Schematic diagram illustrating the mechanisms of IMOD-induced DCs maturation. (G) Intracellular ROS levels in DC2.4 cells after the indicated treatments. (H-K) Bulk RNA sequencing analysis of IMOD-treated and control DC2.4 cells, including pathway activity scores (H), immune-related gene expression (I), differentially expressed genes (J), and Gene Ontology enrichment of up-regulated genes (K). (L-M) Western blot analysis of NF-κB (L) and cGAS-STING (M) signaling pathways. (N) ELISA quantification of IFN-β secretion. (O) Effects of NF-κB and STING inhibition on IMOD-induced DC maturation. n = 3 independent biological replicates. *$P < 0.05$, **$P < 0.01$, ***$P < 0.001$.

3.5. IMOD NAs promotes DCs maturation and migration and enhances cytotoxic T cell responses.

We next examined whether IMOD-driven signaling translated into functional DC activation. Flow cytometry showed a stepwise increase in the proportion of $CD80^+CD86^+$ DC2.4 cells after treatment with OVA, IMO, and IMOD NAs. IMOD NAs produced the strongest response and increased the mature DC population to approximately 68% (Figure 5A-B and Figure S6). These results confirmed that IMOD NAs efficiently promoted DC maturation. Mature DCs exhibited characteristic morphological changes, including increased cell spreading and formation of dendritic protrusions (Figure S5). Mature DCs must migrate to lymphoid tissues to initiate adaptive immunity. We therefore assessed the expression of CCR7, a key receptor that directs DC trafficking. IMOD NAs increased the proportion of $CCR7^+$ DC2.4 cells to approximately 62%, which was higher than that induced by IMO or free OVA (**Figure** 5C-D). Immunofluorescence imaging showed the same trend. IMOD-treated cells displayed the strongest CCR7 signal (Figure 5E, G). Western blot (WB) analysis further demonstrated that IMOD NAs treatment significantly upregulated CCR7 expression (Figure S7C, D). The

increased CCR7 expression was accompanied by enhanced cell motility. In the scratch assay, IMOD NAs induced the greatest wound closure at 12 and 24 hours (Figure 5F, H). Quantification confirmed a higher migration rate than that observed in all other groups (Figure 5H). The Transwell assay further corroborated these findings (Figure S7A-B) Thus, IMOD NAs promoted both phenotypic maturation and migratory competence in DC2.4 cells.

We then evaluated whether these activated DCs could prime cytotoxic T cell responses (Figure 5I). Primary mouse $CD8^+$ T cells were stimulated with DCs subjected to the indicated treatments. IMOD-treated DCs induced the highest expression of perforin and granzyme B in the resulting cytotoxic T lymphocytes (CTLs) (Figure 5J). These molecules mediate targeT cell lysis and are key effectors of CTL activity. IMOD NAs also enhanced the proliferation of both CTLL-2 cells and primary $CD8^+$ T cells, as shown by EdU incorporation (Figure 5K, M). No significant difference was observed between the two T cell models within each treatment group. This result indicated a consistent proliferative response to IMOD-activated DCs.

The functional activity of the primed T cells was further assessed. IFN-γ ELISpot analysis showed a marked increase in the number of IFN-γ-secreting T cells after stimulation with IMOD-treated DCs (Figure 5N, O). This response exceeded that induced by IMO and free OVA. Consistently, CTLs primed by IMOD-treated DCs caused extensive tumor cell death. Live/dead staining showed a pronounced loss of viable tumor cells and a corresponding increase in PI-positive cells (Figure 5L). Quantification confirmed the highest tumor cell death rate in the IMOD group (Figure 5P).

Together, these results show that IMOD NAs promotes DC maturation and CCR7-dependent migratory activity. It also enhances T cell expansion, effector-molecule production, IFN-γ secretion, and tumor-cell killing. IMOD NAs therefore converts DC activation into a potent cytotoxic T cell response.

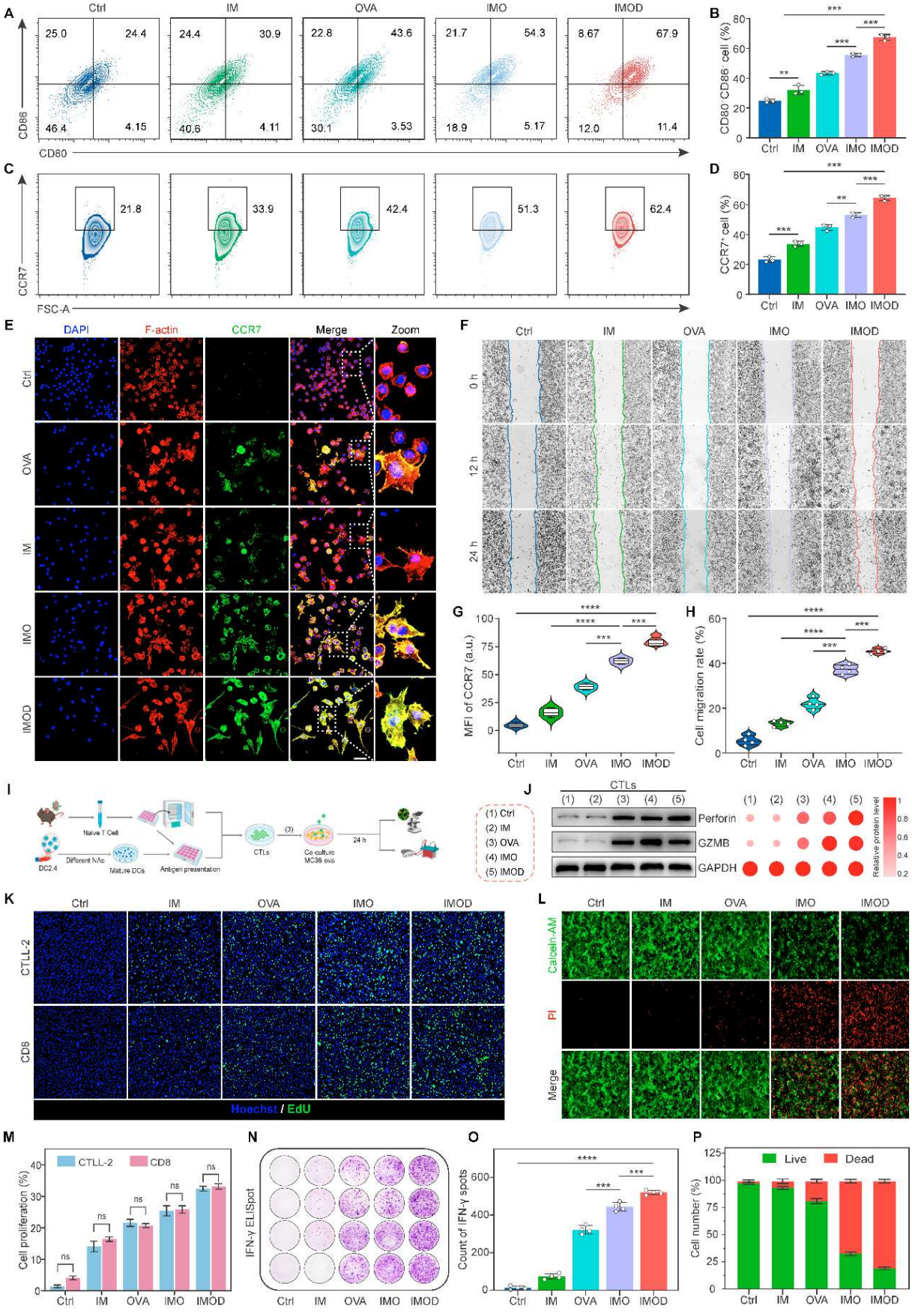


Figure 5. IMOD NAs enhances DC migration and primes cytotoxic T cell responses. (A-B) Representative flow cytometry plots and quantification of $CD80^{+}CD86^{+}$ DC2.4 cells after the

indicated treatments. (C-D) Representative flow cytometry plots and quantification of $CCR7^+$ DC2.4 cells. (E) Representative immunofluorescence images of CCR7 expression in DC2.4 cells. Nuclei, DAPI (blue); F-actin, red; CCR7, green. (F) Representative scratch-wound images of DC2.4 cell migration at 0, 12, and 24 hours. (G) Quantification of CCR7 mean fluorescence intensity in (E). (H) Quantification of the cell migration rate in (F). (I) Schematic of primary mouse $CD8^+$ T cell activation by treated DC2.4 cells and the subsequent tumor cell-killing assay. (J) Western blot and densitometric analyses of perforin and granzyme B (GZMB) expression in cytotoxic T lymphocytes (CTLs). GAPDH served as the loading control. (K) Representative EdU staining images showing the proliferation of CTLL-2 and primary $CD8^+$ T cells after the indicated treatments. Nuclei, Hoechst (blue); EdU, green. (L) Calcein-AM/propidium iodide staining of tumor cells after coculture with activated $CD8^+$ T cells. Live cells, green; dead cells, red. (M) Quantification of CTLL-2 and $CD8^+$ T cell proliferation in (K). (N-O) Representative IFN-γ ELISpot images and corresponding spot counts for activated $CD8^+$ T cells. (P) Quantification of live and dead tumor cells in (L). Data are presented as means ± SD. ns, not significant; $*P < 0.05$, $**P < 0.01$, $***P < 0.001$.

3.6. Targeting ability and imaging of IMOD NAs *in vivo*

Efficient delivery to draining lymph nodes (dLNs) is critical for local activation of antigen-presenting cells. We therefore examined the *in vivo* fate of IMOD NAs after footpad administration. Cy5.5-labeled IMO and IMOD NAs were monitored by longitudinal fluorescence imaging. IMO showed an early increase in fluorescence, which peaked at approximately 4 hours and then rapidly declined. In contrast, the IMOD NAs signal increased progressively and reached a maximum at 10 to 12 hours. A strong signal remained detectable at 24 hours (**Figure** 6A, D). These distinct kinetics indicate that DC membrane coating prolonged the retention of IMOD NAs and favored its transport toward the lymphatic compartment. We next examined the tissue distribution at 12 hours after injection. *Ex vivo* imaging revealed strong fluorescence in the dLNs of IMOD-treated mice. The corresponding

signal was much weaker after IMO administration (Figure 6B, C). Imaging of isolated lymph nodes yielded a similar pattern. IMOD NAs produced markedly higher fluorescence than IMO (Figure 6E). These results confirmed efficient accumulation of IMOD NAs in the dLNs. TEM images of lymph nodes following IMOD NAs treatment revealed the successful uptake of IMOD NAs by lysosomes and its subsequent escape from lysosomal compartments (Figure S9). We then asked whether the enhanced lymph node delivery increased nanoparticle uptake by DCs. Flow cytometry showed a pronounced increase in Cy5.5-positive $CD11c^+$ cells after IMOD NAs administration. Approximately 22.8% of $CD11c^+$ cells were Cy5.5 positive in the IMOD group, compared with 3.23% in the IMO group (Figure 6F and Figure S8). Quantification confirmed this difference ($P < 0.0001$; Figure 6I). Thus, DC membrane coating markedly enhanced the delivery of IMOD NAs to DCs within the dLNs.

The biodistribution of Mn and Ir was further quantified to track the components of IMOD NAs. Both elements accumulated in the dLNs at 12 hours and remained detectable at 60 hours (Figure 6G, H). Their tissue levels decreased over time, indicating gradual clearance. The liver showed the highest systemic accumulation, whereas appreciable amounts of both Mn and Ir were retained in the dLNs during the early phase after administration. These data establish that IMOD NAs efficiently reaches the dLNs and is readily captured by resident DCs. This lymph node-directed delivery provides a favorable basis for subsequent DC activation and antigen-specific immune priming.

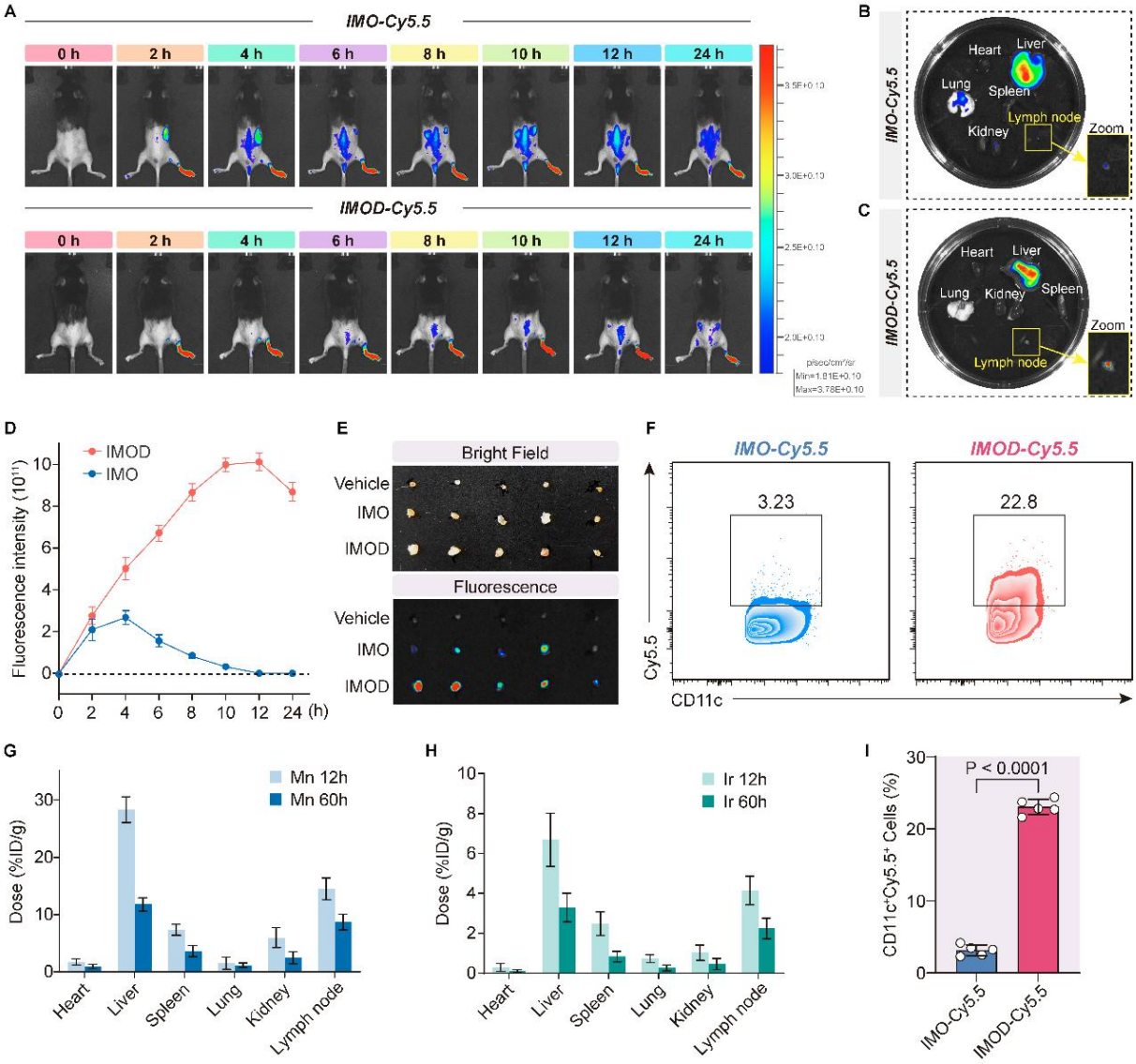


Figure 6. IMOD NAs enhances lymph node accumulation and DCs uptake in vivo. (A) Time-dependent in vivo fluorescence imaging of mice after footpad injection of Cy5.5-labeled IMO or IMOD NAs. (B, C) *Ex vivo* fluorescence images of the draining lymph nodes and major organs collected 12 hours after injection of Cy5.5-labeled IMO (B) or IMOD NAs (C). (D) Quantification of the fluorescence intensity of Cy5.5-labeled IMO and IMOD NAs over time. (E) Representative bright-field and fluorescence images of draining lymph nodes after the indicated treatments. (F) Representative flow cytometry analysis of Cy5.5-labeled IMO and IMOD NAs uptake by $CD11c^+$ DCs in the draining lymph nodes. (G, H) Biodistribution of Mn (G) and Ir (H) in major organs and draining lymph nodes at 12 and 60 hours after administration, expressed as percentage of injected dose per gram of tissue (%ID/g). (I) Quantification of

$CD11c^+Cy5.5^+$ cells in the draining lymph nodes corresponding to (F). Data are presented as means ± SD. Statistical significance is indicated in the figure.

3.7. In vivo antitumor efficacy of IMOD NAs combined with αPD-L1.

The antitumor efficacy of IMOD NAs was evaluated in MC38-Luc-OVA tumor-bearing mice (**Figure** 7A). Tumor progression was followed by longitudinal bioluminescence imaging. Rapid tumor expansion was observed in PBS-treated mice. αPD-L1 or IMO alone produced only partial tumor control. IMOD NAs was substantially more effective. Tumor-associated bioluminescence remained markedly lower throughout treatment (Figure 7B, C). Notably, the addition of αPD-L1 further strengthened this response. IMOD plus αPD-L1 produced the weakest tumor signal among all treatment groups.

This therapeutic advantage was also evident at the endpoint. Tumors from IMOD-treated mice were markedly smaller than those from mice receiving IMO (Figure 7D). αPD-L1 further enhanced the efficacy of IMOD NAs and yielded the lowest tumor weight (Figure 7E). Individual growth curves reinforced this trend. Tumors progressed rapidly in the PBS group and remained poorly controlled by αPD-L1 alone. IMO delayed tumor growth to a limited extent. By contrast, IMOD NAs produced sustained growth suppression. The combination of IMOD and αPD-L1 achieved the most durable tumor control (Figure 7F). This benefit translated into prolonged survival (Figure 7G). Meanwhile, body weight remained largely unchanged across all groups (Figure 7H). These data indicate potent antitumor activity without overt treatment-associated toxicity.

Histological analyses further revealed the extent of tumor destruction. H&E staining showed progressively increased tissue damage after IMOD-based treatment (Figure 7I). In parallel, Ki67-positive tumor cells were markedly reduced. The lowest proliferative fraction was observed in the IMOD+αPD-L1 group (Figure 7I, K). TUNEL staining showed the opposite pattern. IMOD NAs increased tumor cell death, and αPD-L1 further amplified this effect (Figure 7I, L). Thus, the superior tumor control was accompanied by both impaired tumor

proliferation and enhanced tumor cell elimination.

The immune basis of this response was then examined within the tumor microenvironment. IMOD NAs markedly increased the infiltration of $CD8^+$ T cells (Figure 7J). It also enhanced granzyme B expression, indicating greater cytotoxic activity. This response was further intensified by αPD-L1. Accordingly, tumors from the combination group contained the highest proportion of $CD8^+GZMB^+$ cells (Figure 7M). These findings suggest that IMOD NAs reshaped the tumor immune microenvironment toward a cytotoxic phenotype and sensitized tumors to PD-L1 blockade. Together, IMOD NAs elicited strong tumor suppression as a monotherapy and further potentiated αPD-L1 treatment. The combination produced durable tumor control, extended survival, and reinforced intratumoral cytotoxic T cell responses.

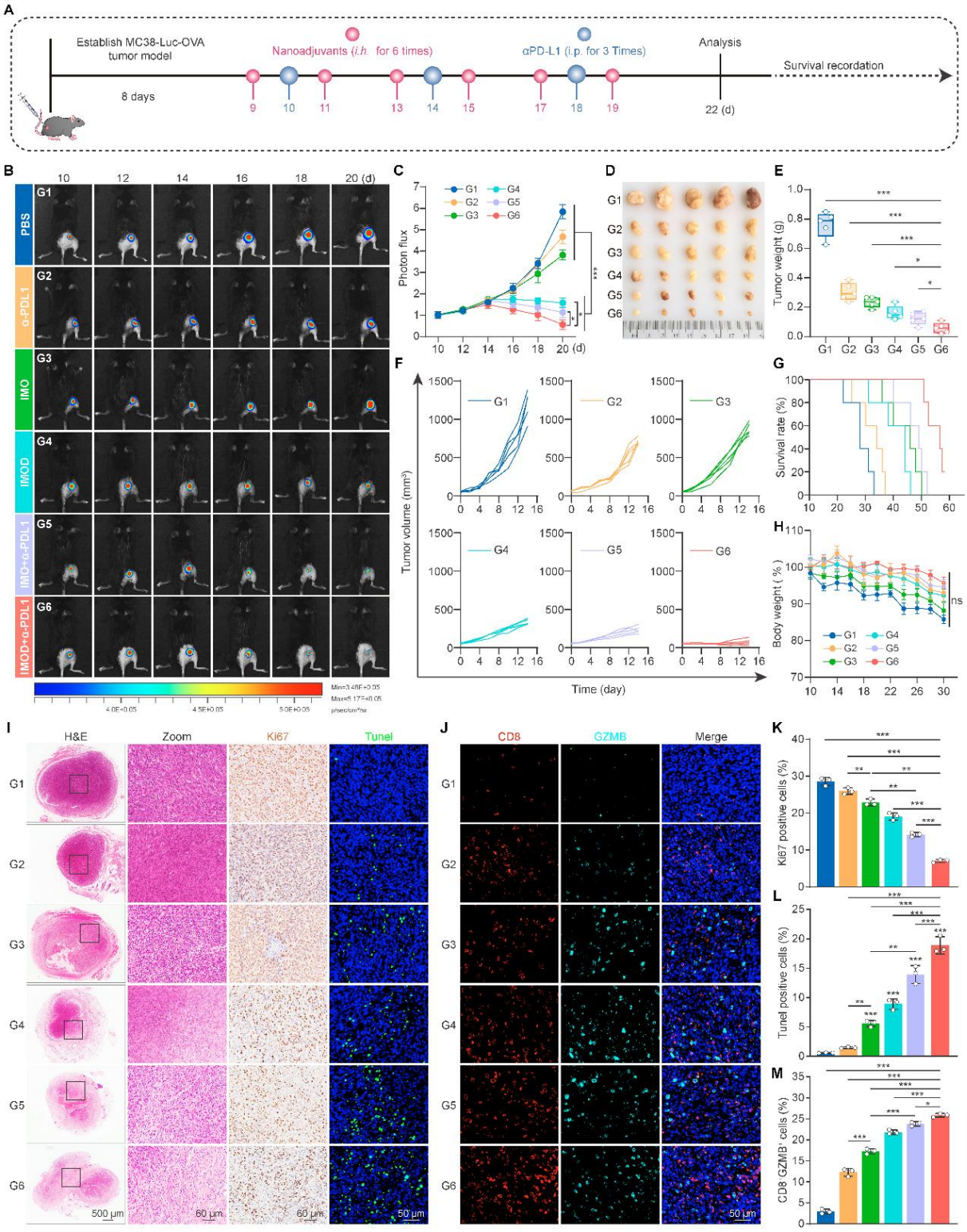


Figure 7. *In vivo* antitumor efficacy of IMOD NAs combined with αPD-L1. (A) Schematic of the treatment schedule in the MC38-Luc-OVA tumor model. Mice received PBS (G1), αPD-L1 (G2), IMO (G3), IMOD (G4), IMO+αPD-L1 (G5), or IMOD+αPD-L1 (G6). (B) Representative bioluminescence images of tumor-bearing mice during treatment. (C) Quantification of tumor-

associated photon flux in (B). (D, E) Excised tumors (D) and corresponding tumor weights (E) at the endpoint. (F) Individual tumor growth curves for each treatment group. (G) Survival curves of MC38-Luc-OVA-bearing mice exposed to the indicated treatments (H) Changes in body weight during treatments. (I) Representative H&E staining and immunohistochemical or fluorescence staining of Ki67 and TUNEL in tumor sections. (J) Representative immunofluorescence images of CD8 and granzyme B (GZMB) in tumor tissues. (K, L) Quantification of Ki67-positive cells (K) and TUNEL-positive cells (L) in tumor sections. (M) Quantification of $CD8^+GZMB^+$ cells in tumor tissues. Scale bars, 500 μm for whole-tumor H&E images, 60 μm for enlarged H&E and Ki67 images, and 50 μm for TUNEL and immunofluorescence images. Statistical significance is indicated in the figure. ns, not significant; $n = 5$ mice. $^*P < 0.05$, $^{**}P < 0.01$, $^{***}P < 0.001$.

3.8. IMOD NAs reprograms TDLN to enhance antitumor immunity

Tumor-draining lymph nodes (TDLNs) are the principal sites where tumor antigens are presented and antitumor T cell responses are initiated. We therefore examined whether IMOD NAs altered the immune state of TDLNs. Flow cytometry revealed a clear increase in mature $CD11c^+CD80^+CD86^+$ DCs after IMOD NAs treatment (**Figure** 8A-B, and Figure S10). This response was stronger than that induced by IMO. Notably, αPD-L1 further enhanced IMOD-induced DCs maturation. The combination produced the highest frequency of mature DCs among all groups. Thus, IMOD NAs efficiently promoted DC activation in vivo, and this effect was reinforced by checkpoint blockade. DC maturation was accompanied by increased CCR7 expression. IMO produced only a moderate increase in $CCR7^+$ DCs. By contrast, IMOD NAs induced a substantially larger $CCR7^+$ population (Figure 8C-D and Figure S10). The response was further amplified by αPD-L1. The combination group reached the highest level of $CCR7^+$ DCs. These data indicate that IMOD NAs not only activated DCs but also promoted a phenotype associated with lymphoid migration and T cell priming. This enhanced DC response was followed by marked remodeling of the T cell compartment. IMOD NAs increased the

abundance of effector T cells in TDLNs, with a prominent expansion of the $CD8^+$ population (Figure 8E-F and Figure S11). Again, αPD-L1 strengthened this effect. In sharp contrast, the immunosuppressive Treg compartment contracted. $CD4^+FOXP3^+$ Tregs accounted for approximately 27% of the corresponding T cell population in PBS-treated mice. This fraction fell to ~11% after IMOD NAs treatment and to ~3% after IMOD+αPD-L1 treatment (Figure 8G-H and Figure S11). Thus, IMOD NAs shifted the local immune balance from suppression toward activation. PD-L1 blockade further intensified this shift.

Multiplex immunofluorescence revealed the spatial basis of this immune remodeling. IMOD NAs increased the abundance of $CD11c^+$ and MHC-I antigen-presenting cells within TDLNs (Figure 8I). $CD8^+$ T cells accumulated in parallel. GZMB signals also increased, indicating enhanced cytotoxic activation. These changes were most prominent in the IMOD+αPD-L1 group. Conversely, $FOXP3^+$ cells were markedly reduced. This reciprocal increase in cytotoxic immunity and loss of regulatory suppression was consistent with the flow cytometric findings. Histological analyses further supported these observations. H&E staining showed pronounced structural changes in TDLNs after immunotherapy (Figure 8J). More importantly, CD8 immunohistochemistry revealed a progressive increase in $CD8^+$ cell infiltration across the treatment groups (Figure 8K-L). IMOD NAs induced substantially greater $CD8^+$ T cell accumulation than IMO. αPD-L1 further enhanced this response, yielding the highest $CD8^+$ cell density in the combination group. Collectively, IMOD NAs transformed TDLNs into an immunologically active niche. It promoted DC maturation and CCR7 expression, strengthened antigen-presenting activity, expanded cytotoxic T cells, and restrained Treg accumulation. αPD-L1 amplified each of these responses.

Furthermore, immunofluorescence analysis of lymph node sections revealed enhanced STING/NF-κB signaling activation in $CD11c^+$ DCs following different treatments. Compared with the PBS group, IMOD, αPD-L1, and their combination increased the phosphorylation levels of STING and NF-κB p65, as indicated by elevated p-STING and p-NF-κB p65 signals.

Notably, the IMOD+αPD-L1 group exhibited the most pronounced activation of both pathways, with enhanced colocalization of CD11C with p-STING and p-NF-κB p65. These findings indicate that IMOD NAs promotes DC activation through STING/NF-κB pathway engagement and contributes to immune microenvironment remodeling (Figure S12). This coordinated remodeling of the TDLN immune landscape provides a mechanistic link between IMOD-mediated immune priming and the superior antitumor efficacy of the combination therapy.

To assess the biosafety of IMOD NAs for intravenous administration, hemolysis assays were initially performed. After 3 h of incubation, no obvious erythrocyte deformation, membrane disruption, or aggregation was observed, indicating the excellent hemocompatibility of IMOD NAs *in vitro* (Figure S13C). Furthermore, blood biochemical and hematological analyses revealed no significant differences among the treatment groups in liver and kidney function markers, including ALT, AST, CRE, and BUN, or in hematological parameters, including RBC, WBC, PLT, and HGB (Figure S13B). In addition, H&E staining of major organs (heart, liver, spleen, lung, and kidney) showed preserved tissue architecture without detectable pathological abnormalities (Figure S13A). Collectively, these results demonstrate the favorable in vivo biocompatibility of IMOD NAs, supporting its potential for further biomedical applications.

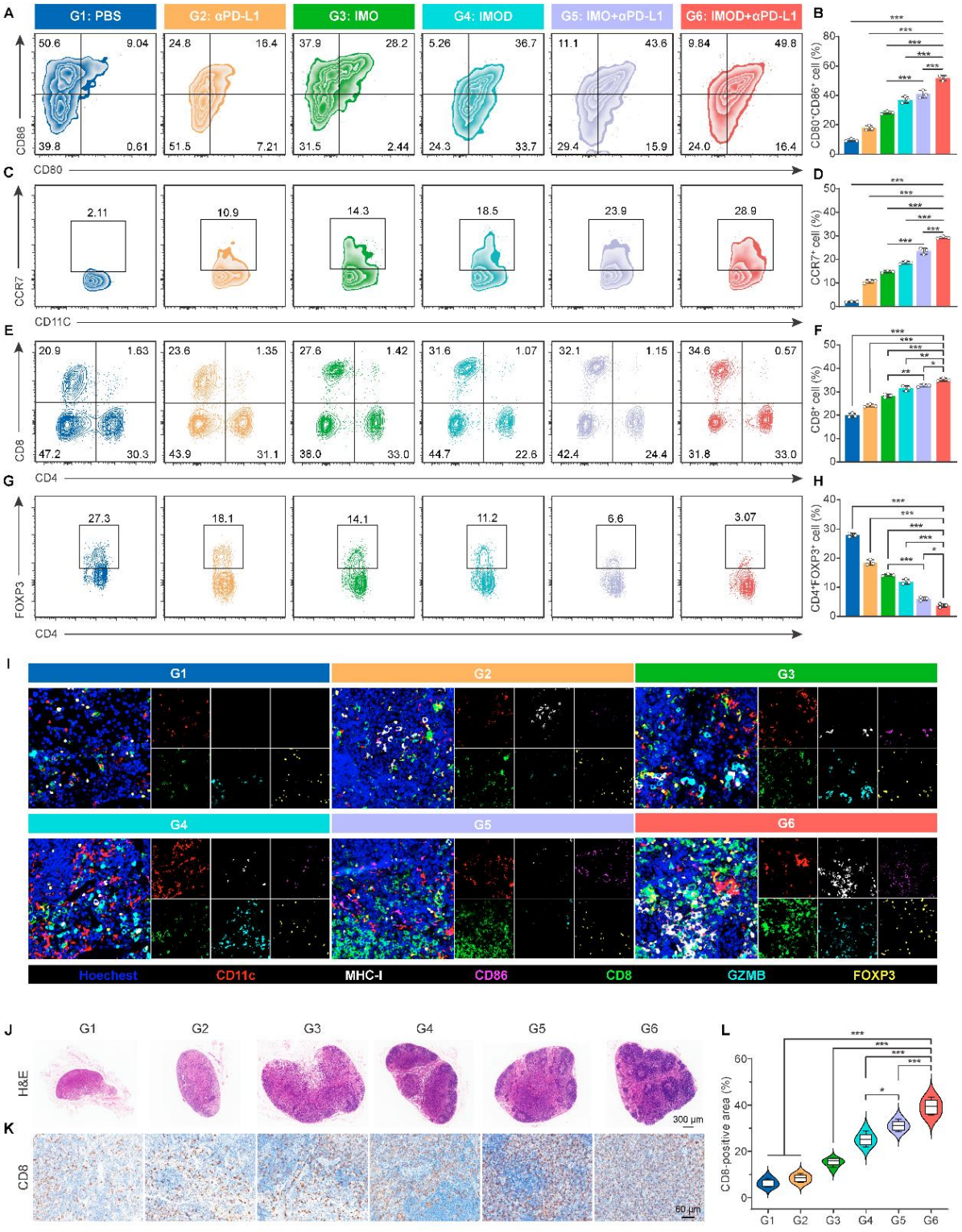


Figure 8. IMOD NAs enhances immune activation in tumor-draining lymph nodes. (A-B) Representative flow cytometry plots (A) and quantification (B) of mature $CD11c^{+}CD80^{+}CD86^{+}$ DCs in tumor-draining lymph nodes (TDLNs) after the indicated treatments. (C-D) Representative flow cytometry plots (C) and quantification (D) of $CD11c^{+}CCR7^{+}$ DCs in TDLNs. (E-F) Representative flow cytometric analysis of $CD4^{+}$ and $CD8^{+}$ T cell populations

(E) and quantification of $CD8^+$ T cells (F) in TDLNs. (G-H) Representative flow cytometry plots (G) and quantification (H) of $CD4^+FOXP3^+$ regulatory T cells (Tregs) in TDLNs. (I) Multiplex immunofluorescence analysis of the immune microenvironment in TDLNs after the indicated treatments. (J) Representative H&E staining of TDLNs. Scale bar, 500 μm. (K) Representative immunohistochemical staining of $CD8^+$ cells in TDLNs. Scale bar, 50 μm. (L) Quantification of $CD8^+$ cells in (K). G1, PBS; G2, anti-PD-L1; G3, IMO; G4, IMOD; G5, IMO plus anti-PD-L1; G6, IMOD plus anti-PD-L1. Statistical significance is indicated in the figure. *ns*, not significant*;* $n = 5$ mic*e.* $^*P < 0.05$*,* $^{**}P < 0.01$*,* $^{***}P < 0.001$.

3. Discussion

The clinical success of cancer immunotherapy has fundamentally changed the landscape of cancer treatment[3, 31]. However, durable responses remain limited in many solid tumors, including colorectal cancer[32]. One major reason is that effective antitumor immunity is not simply determined by the presence of immune cells within tumors, but rather by whether immune responses can be properly initiated and sustained[33]. Tumor-draining lymph nodes (TDLNs) serve as the central command centers for this process. Here, tumor-derived antigens are captured, processed, and presented to naïve lymphocytes, ultimately determining the magnitude and quality of tumor-specific immunity[34-35]. Nevertheless, during tumor progression, TDLNs are frequently remodeled into dysfunctional immune niches, characterized by impaired DC activation, insufficient antigen presentation, and expansion of immunosuppressive populations[36-38]. Therefore, restoring the immune-initiating capacity of TDLNs represents an attractive yet largely unexplored strategy to improve cancer immunotherapy.

In this study, by integrating single-cell RNA sequencing and bulk transcriptomic analysis of human colorectal cancer TDLNs, we identified a distinct $LAMP3^+$ aDC population associated with immune activation. Unlike conventional DC subsets that primarily perform antigen processing and presentation, $LAMP3^+$ aDCs displayed a broader immunostimulatory phenotype.

They exhibited elevated expression of costimulatory molecules, enhanced MHC-I antigen presentation capacity, and enrichment of inflammatory signaling pathways, including TNF-NF-κB, interferon responses, Toll-like receptor signaling, and CD40 activation. More importantly, the abundance of these aDCs was closely associated with cGAS-STING pathway activity and oxidative stress-related programs. These observations suggest that activated DC states within TDLNs are shaped by coordinated regulation of innate immune sensing and cellular metabolic adaptation. Thus, $LAMP3^+$ aDCs represent not merely a transcriptional subtype, but a functional immune state capable of orchestrating effective antitumor immunity.

The biological significance of $LAMP3^+$ aDCs became further evident when examining their interaction with lymphocyte populations. TDLNs enriched with aDCs exhibited a profound remodeling of the T cell compartment, with reduced naïve T cell signatures and increased accumulation of antigen-experienced effector populations. This transition reflects an active immune-priming environment rather than a passive expansion of immune cells. Cell-cell communication analysis revealed that aDCs occupied a central position within the DC-T cell interaction network. Through coordinated CCL19-CCR7 chemotactic signaling, CD80/CD86-CD28 costimulation, and MHC-I-CD8 antigen recognition, aDCs were predicted to facilitate T cell recruitment, activation, and functional differentiation. These findings provide a mechanistic explanation for how specific DC states within lymphoid tissues can shape systemic antitumor immunity.

Inspired by this endogenous immunostimulatory DC phenotype, we developed a DC membrane-coated iridium-manganese oxide nanoadjuvant (IMOD) to recreate and amplify the immune properties of $LAMP3^+$ aDCs. Although nanomedicine has provided powerful tools for cancer immunotherapy, many existing platforms remain limited by inefficient lymphoid delivery and insufficient activation of antigen-presenting cells. Effective immune modulation requires more than antigen transport. It requires precise delivery to immune niches, appropriate innate immune stimulation, and durable functional reprogramming of immune cells. IMOD

NAs was designed to address these challenges through a biomimetic and multifunctional strategy. The DC membrane coating endowed IMOD NAs with homologous recognition capability and enhanced lymph node targeting. The OVA component provided antigenic stimulation, whereas the iridium-manganese oxide core served as an intrinsic immunoregulatory module.

The immune activation mechanism of IMOD NAs was based on the coordinated engagement of two complementary innate signaling pathways. Upon cellular internalization, IMOD NAs disrupted redox homeostasis by consuming intracellular glutathione, resulting in controlled ROS accumulation and subsequent NF-κB activation. Meanwhile, acid-responsive Mn^{2+} release triggered the STING-TBK1-IRF3 axis and promoted type I interferon production. These two pathways converged to drive DC maturation and enhance antigen-presenting function. Importantly, inhibition of either NF-κB or STING signaling substantially attenuated IMOD-induced DC activation, demonstrating that the therapeutic effect relied on pathway coordination rather than activation of a single immune signal. This dual-input design provides a rational approach for overcoming the intrinsic activation barriers of tumor-associated DCs.

Beyond inducing molecular activation, IMOD NAs successfully converted DC maturation into functional adaptive immunity. Mature DCs must not only express activation markers but also acquire migratory capacity and efficiently prime tumor-specific T cells. IMOD NAs enhanced CCR7 expression and promoted DC migration, suggesting improved trafficking toward lymphoid tissues. Following antigen presentation, IMOD-activated DCs induced robust $CD8^+$ T cell expansion and functional differentiation. These T cells displayed increased expression of perforin and granzyme B, enhanced IFN-γ secretion, and stronger tumor-cell killing activity. Therefore, IMOD NAs does not simply stimulate DC activation in isolation; it establishes a continuous immune cascade from antigen delivery and innate sensing to cytotoxic lymphocyte generation.

A critical challenge for immunomodulatory nanomaterials is achieving sufficient

accumulation at immune initiation sites. Most nanoparticles administered in vivo experience limited lymphatic transport and rapid systemic clearance. The biomimetic architecture of IMOD NAs effectively addressed this limitation. Through DC membrane-mediated recognition, IMOD NAs exhibited prolonged retention in draining lymph nodes and enhanced uptake by resident DCs. This feature is particularly important because the quality of immune priming depends on the local concentration and duration of antigen and adjuvant exposure within lymphoid tissues. By directing immunostimulatory signals to TDLNs, IMOD NAs provides a strategy to manipulate immune responses at their origin rather than only attempting to restore immunity after tumor infiltration.

The therapeutic relevance of TDLN remodeling was demonstrated in vivo. IMOD NAs achieved substantial tumor suppression as a monotherapy and further enhanced the efficacy of αPD-L1 blockade. This improvement was accompanied by coordinated immune remodeling at both tumor and lymphoid sites. Within tumors, IMOD NAs promoted $CD8^+$ T cell infiltration and increased granzyme B expression, indicating enhanced cytotoxic activity. Within TDLNs, IMOD NAs increased mature DC populations, promoted CCR7 expression, expanded effector T cells, and reduced regulatory T cell accumulation. Notably, αPD-L1 further amplified these effects. These results highlight the complementary roles of immune priming and immune reinvigoration: IMOD NAs strengthens the generation of tumor-reactive lymphocytes, whereas checkpoint blockade restores their activity within the tumor microenvironment.

This work establishes a conceptual framework in which human immune profiling guides the development of next-generation immunomodulatory nanomaterials. Rather than designing nanoparticles solely based on physicochemical properties, we identified an endogenous immune state and engineered a synthetic system to reproduce its functional characteristics. The strategy integrates biomimetic targeting, antigen delivery, redox regulation, and innate immune activation within a single platform. More broadly, our findings emphasize that immune organs beyond the tumor itself represent important therapeutic targets. Reprogramming TDLNs may

provide a complementary approach to conventional tumor-centered immunotherapy by improving the quality of immune initiation.

Several questions remain to be addressed before clinical translation. The diversity and stability of activated DC states across different tumor types require further investigation in larger patient cohorts. The long-term biological fate and safety profile of metal-containing nanomaterials also warrant comprehensive evaluation. Nevertheless, this study provides a mechanistically guided strategy for transforming immune niches through rational nanomaterial design. By converting TDLNs into active immune-priming environments, IMOD NAs offers a promising avenue for enhancing checkpoint blockade and developing more effective cancer immunotherapies.

5. Conclusion

In this study, we established a human immune-state-guided strategy for engineering biomimetic nanoadjuvants to enhance antitumor immune priming within TDLNs. Integrated single-cell and bulk transcriptomic analyses of human colorectal cancer TDLNs identified a $LAMP3^+$ activated DC state associated with enhanced antigen presentation, innate immune activation, and antigen-experienced $CD8^+$ T cell responses. Guided by these findings, we developed IMOD NAs that enhanced TDLN targeting and antigen delivery while coordinately activating ROS–NF-κB and Mn^{2+}-dependent STING signaling. Excitingly, IMOD NAs enhanced DC maturation, migration, and antigen presentation, leading to increased cytotoxic $CD8^+$ T cell priming and reduced regulatory T cell accumulation within TDLNs. Significantly, IMOD NAs effectively suppressed tumor growth and potentiated the therapeutic efficacy of PD-L1 blockade. Collectively, these findings highlight the therapeutic potential of targeting immune initiation within TDLNs and provide a promising framework for translating human immune profiling into rational nanoadjuvant design to improve cancer immunotherapy.

Acknowledgements

This paper was supported by the National Natural Science Foundation of China (grant number 82473407,82573619), and the Science and Education Cultivation Fund of the National Cancer and Regional Medical Centre of Shanxi Provincial Cancer Hospital (grant numbers TD2023001). Figure 5I was created with BioRender.com (Publication License granted to the author).

Authors contributions

Xin Zhang: Writing-Original draft, Methodology, Investigation. Tiantongfei Jiang: Writing-Original draft, Methodology, Investigation. Lingxiao Zhao: Writing-Reviewing and Editing. Yuxin Wan: Data curation, Formal analysis, Investigation. Chan Li: Resources, Methodology. Yaru Niu: Resources, Investigation. Jian Ma: Supervision. Juan Xu: Investigation, Resources, Supervision. Xu Guan: Conceptualization, Funding acquisition, Investigation, Writing-review & editing. Xishan Wang: Funding acquisition, Project administration, Supervision. All authors have read and approved the final manuscript.

Declaration of competing interest

The authors declare that they have no competing interests.

Ethical statement

The study was conducted in accordance with the Declaration of Helsinki and relevant national guidelines for research involving human specimens. Lymph node (LN) tissues were collected from surgical specimens by experienced surgeons and pathologists. Written informed consent was obtained from all participants for the use of tissue specimens and the reporting and sharing of deidentified individual-level data. The study protocol was reviewed and approved by the institutional review boards of the National Cancer Center/Cancer Hospital, Chinese Academy of Medical Sciences and Peking Union Medical College (Approval No. 24/571-4851). The study complied with the requirements for the review and approval of human genetic

resources in China, and the use and export of genetic and sequencing data were approved by the Ministry of Science and Technology of China (Approval No. 2026BAT00508).

This study was approved by the Ethics Committee for Experimental Animal Welfare of China Medical University (CMU20260385).

Data and code availability

Raw RNA-seq data derived from human samples have been deposited at the Genome Sequence Archive in National Genomics Data Center, China National Center for Bioinformation/Beijing Institute of Genomics, Chinese Academy of Sciences, under accession number GSA-Human: HRA010982 and HRA016021.

This paper does not report original code.

Any additional information required to reanalyze the data reported in this paper is available from the lead contact upon request.

References

[1] Hegde PS, Chen DS. Top 10 challenges in cancer immunotherapy. Immunity. 2020;52(1):17–35.

[2] Waldman AD, Fritz JM, Lenardo MJ. A guide to cancer immunotherapy: from T cell basic science to clinical practice. Nat Rev Immunol. 2020;20(11):651–668.

[3] Hiam-Galvez KJ, Allen BM, Spitzer MH. Systemic immunity in cancer. Nat Rev Cancer. 2021;21(6):345–359.

[4] Dammeijer F, van Gulijk M, Mulder EE, Lukkes M, Klaase L, van den Bosch T, et al. The PD-1/PD-L1-checkpoint restrains T cell immunity in tumor-draining lymph nodes. Cancer Cell. 2020;38(5):685–700.e8.

[5] Connolly KA, Kuchroo M, Venkat A, Khatun A, Wang J, William I, et al. A reservoir of stem-like CD8+ T cells in the tumor-draining lymph node preserves the ongoing antitumor immune response. Sci Immunol. 2021;6(64).

[6] Prokhnevska N, Cardenas MA, Valanparambil RM, Sobierajska E, Barwick BG, Jansen C, et al. CD8+ T cell activation in cancer comprises an initial activation phase in lymph nodes followed by effector differentiation within the tumor. Immunity. 2023;56(1):107–124.e5.

[7] Delclaux I, Ventre KS, Jones D, Lund AW. The tumor-draining lymph node as a reservoir for systemic immune surveillance. Trends Cancer. 2024;10(1):28–37.

[8] Cruz de Casas P, Knöpper K, Dey Sarkar R, Kastenmüller W. Same yet different—how lymph node heterogeneity affects immune responses. Nat Rev Immunol. 2024;24(5):358–374.

[9] Guan X, Zhang Y, Sun R, Wang G, Bi X, Zhang Z, et al. Lymph nodes molecular subtypes unravel lymph nodes heterogeneity and clinical implications in colorectal cancer. Nat Commun. 2025;16(1):7834.

[10] Wculek SK, Cueto FJ, Mujal AM, Melero I, Krummel MF, Sancho D. Dendritic cells in cancer immunology and immunotherapy. Nat Rev Immunol. 2020;20(1):7–24.

[11] Garris CS, Arlauckas SP, Kohler RH, Trefny MP, Garren S, Piot C, et al. Successful anti-PD-1 cancer immunotherapy requires T cell-dendritic cell crosstalk involving the cytokines IFN-γ and IL-12. Immunity. 2018;49(6):1148–1161.e7.

[12] Binnewies M, Mujal AM, Pollack JL, Combes AJ, Hardison EA, Barry KC, et al. Unleashing type-2 dendritic cells to drive protective antitumor CD4+ T cell immunity. Cell. 2019;177(3):556–571.e16.

[13] Maier B, Leader AM, Chen ST, Tung N, Chang C, LeBerichel J, et al. A conserved dendritic-cell regulatory program limits antitumour immunity. Nature. 2020;580(7802):257–262.

[14] Zhang Q, He Y, Luo N, Patel SJ, Han Y, Gao R, et al. Landscape and dynamics of single immune cells in hepatocellular carcinoma. Cell. 2019;179(4):829–845.e20.

[15] Cheng S, Li Z, Gao R, Xing B, Gao Y, Yang Y, et al. A pan-cancer single-cell transcriptional atlas of tumor infiltrating myeloid cells. Cell. 2021;184(3):792–809.e23.

[16] Gerhard GM, Bill R, Messemaker M, Klein AM, Pittet MJ. Tumor-infiltrating dendritic cell states are conserved across solid human cancers. J Exp Med. 2021;218(1).

[17] Shapir Itai Y, Barboy O, Salomon R, Bercovich A, Xie K, Winter E, et al. Bispecific dendritic-T cell engager potentiates anti-tumor immunity. Cell. 2024;187(2):375–389.e18.

[18] Goldberg MS. Improving cancer immunotherapy through nanotechnology. Nat Rev Cancer. 2019;19(10):587–602.

[19] Riley RS, June CH, Langer R, Mitchell MJ. Delivery technologies for cancer immunotherapy. Nat Rev Drug Discov. 2019;18(3):175–196.

[20] Irvine DJ, Dane EL. Enhancing cancer immunotherapy with nanomedicine. Nat Rev Immunol. 2020;20(5):321–334.

[21] Sun X, Zhang Y, Li J, Park KS, Han K, Zhou X, et al. Amplifying STING activation by cyclic dinucleotide–manganese particles for local and systemic cancer metalloimmunotherapy. Nat Nanotechnol. 2021;16(11):1260–1270.

[22] Wan D, Que H, Chen L, Lan T, Hong W, He C, et al. Lymph-node-targeted cholesterolized TLR7 agonist liposomes provoke a safe and durable antitumor response. Nano Lett. 2021;21(19):7960–7969.

[23] Han X, Wang L, Li T, Zhang J, Zhang D, Li J, et al. Beyond blocking: engineering RNAi-mediated targeted immune checkpoint nanoblocker enables T cell-independent cancer treatment. ACS Nano. 2020;14(12):17524–17534.

[24] Martin JD, Cabral H, Stylianopoulos T, Jain RK. Improving cancer immunotherapy using nanomedicines: progress, opportunities and challenges. Nat Rev Clin Oncol. 2020;17(4):251–266.

[25] Mitchell MJ, Billingsley MM, Haley RM, Wechsler ME, Peppas NA, Langer R. Engineering precision nanoparticles for drug delivery. Nat Rev Drug Discov. 2021;20(2):101–124.

[26] Jiang Y, Krishnan N, Zhou J, Chekuri S, Wei X, Kroll AV, et al. Engineered cell-membrane-

coated nanoparticles directly present tumor antigens to promote anticancer immunity. Adv Mater. 2020;32(30).

[27] Jin L, Yang D, Song Y, Li D, Xu W, Zhu Y, et al. In situ programming of nanovaccines for lymph node-targeted delivery and cancer immunotherapy. ACS Nano. 2022;16(9):15226–15236.

[28] Wang Q, Wang Z, Sun X, Jiang Q, Sun B, He Z, et al. Lymph node-targeting nanovaccines for cancer immunotherapy. J Control Release. 2022;351:102–122.

[29] Pant S, Wainberg ZA, Weekes CD, Furqan M, Kasi PM, Devoe CE, et al. Lymph-node-targeted, mKRAS-specific amphiphile vaccine in pancreatic and colorectal cancer: the phase 1 AMPLIFY-201 trial. Nat Med. 2024;30(2):531–542.

[30] Luo GF, Chen WH, Zeng X, Zhang XZ. Cell primitive-based biomimetic functional materials for enhanced cancer therapy. Chem Soc Rev. 2021;50(2):945–985.

[31] Kubli SP, Berger T, Araujo DV, Siu LL, Mak TW. Beyond immune checkpoint blockade: emerging immunological strategies. Nat Rev Drug Discov. 2021;20(12):899–919.

[32] Ganesh K. Optimizing immunotherapy for colorectal cancer. Nat Rev Gastroenterol Hepatol. 2022;19(2):93–94.

[33] Philip M, Schietinger A. CD8+ T cell differentiation and dysfunction in cancer. Nat Rev Immunol. 2022;22(4):209–223.

[34] du Bois H, Heim TA, Lund AW. Tumor-draining lymph nodes: at the crossroads of metastasis and immunity. Sci Immunol. 2021;6(63).

[35] Jhunjhunwala S, Hammer C, Delamarre L. Antigen presentation in cancer: insights into tumour immunogenicity and immune evasion. Nat Rev Cancer. 2021;21(5):298–312.

[36] van Krimpen A, Huang J, Eterman M, Gerretsen V, Umetani M, Janssen JC, et al. PLA2G2D in tumour-draining lymph nodes regulates anti-tumour immunity. Nature. 2026;658(8135):485–495.

[37] Pittet MJ, Di Pilato M, Garris CS, Mempel TR. Dendritic cells as shepherds of T cell

immunity in cancer. Immunity. 2023;56(10):2218–2230.

[38] Del Prete A, Salvi V, Soriani A, Laffranchi M, Sozio F, Bosisio D, et al. Dendritic cell subsets in cancer immunity and tumor antigen sensing. Cell Mol Immunol. 2023;20(5):432–447.

Supplementary Files

This is a list of supplementary files associated with this preprint. Click to download.

- SupportingInformation.docx